An R&D Program for Targetry at a Muon Collider

A Proposal to the BNL AGS Division

James Alessi,[b] John Corlett,[e] D. Duncan Earl,[f] Richard C. Fernow,[b] Yasuo Fukui,[d]
Tony A. Gabriel,[f] Juan C. Gallardo,[b] Michael A. Green,[e] John R. Haines,[f] JerryHastings,[b]
Ahmed Hassanein,[a] Colin Johnson,[c] Stephen A. Kahn,[b] Bruce J. King,[b] Harold G. Kirk,[b]
Paul Lebrun,[d] Vincent LoDestro,[b] Changguo Lu,[g] Kirk T. McDonald,[g,1]
Nikolai V. Mokhov,[d] James H. Norem,[a] Robert B. Palmer,[b] Eric J. Prebys,[g] Claude Reed,[a]
Thomas Roser,[b] Ronald M. Scanlan,[e] Dale L. Smith,[a] Yağmur Torun,[b,h]
Andy van Ginneken,[d] Haipeng Wang,[b] Robert Weggel,[b] Yongxiang Zhao[b]

[a] *Argonne National Laboratory, Argonne, IL 60439*
[b] *Brookhaven National Laboratory, Upton, NY 11973*
[c] *CERN, 1211 Geneva 23, Switzerland*
[d] *Fermi National Laboratory, P. O. Box 500, Batavia, IL 60510*
[e] *Lawrence Berkeley National Laboratory, 1 Cyclotron Rd., Berkeley, CA 94720*
[f] *Oak Ridge National Laboratory, Oak Ridge, TN 37831*
[g] *Joseph Henry Laboratories, Princeton University, Princeton, NJ 08544*
[h] *Department of Physics and Astronomy, SUNY, Stony Brook, NY 11790*

(DRAFT, August 24, 1998)

[1] Spokesperson. Email: mcdonald@puphep.princeton.edu

Executive Summary

Contents

1 Introduction

1.1 Overview of a Muon Collider

The energy frontier of high energy physics is presently pursued with two types of colliding beam facilities:

- **Proton-proton machines** in which storage rings contain the colliding beams, but for which the constituent (primarily gluon-gluon) center-of-mass (CoM) energy is poorly defined and effectively about 1/10 of the p-p CoM energy.
- **Electron-positron linear colliders** in which all of the CoM energy is available for fundamental process, but for which the effects of quantum beamstrahlung limit the precision of the initial state at high energies and luminosities. An e^+e^- storage ring of CoM energy higher than LEP is not foreseen, due to the high power required to compensate for synchrotron radiation.

Future examples of such machines will be rather costly.

In this context a new type of high energy particle accelerator,

- A **muon collider** [1, 2],

has many attractive features. Muons are leptons, and so like electrons couple directly to fundaental processes. But muons are 200 times heavier than electrons, so initial-state radiation (beamstrahlung and synchrotron radiation) are negligible for CoM energies up to of order 100 TeV. Hence, recirculating accelerators and storage rings can be used at a muon collider, offering cost advantages over both electron-positron and proton-proton colliders.

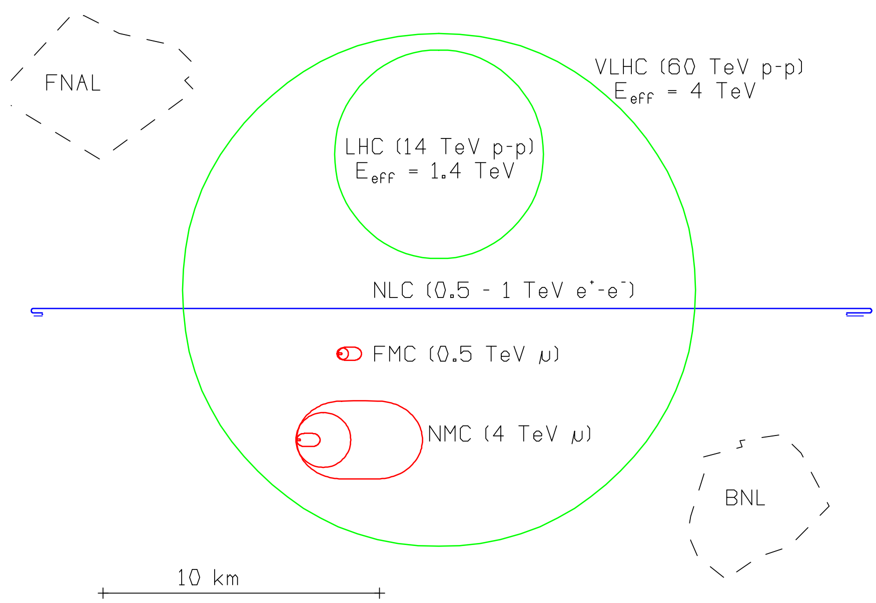

Figure 1: Comparison of footprints of possible future colliders, including a first muon collider (FMC) and a next muon collider (NMC) at 3-4 TeV CoM.

A physics advantage of muons over electrons and protons (*i.e.*, gluons) is that muons have the largest s-channel coupling (which is proportional to m^2) to Higgs-type bosons, permitting precision studies of such particles. A first muon collider might focus on this unique opportunity.

A 3-4-TeV muon collider would fit on the existing sites of BNL or FNAL, as shown in Fig. 1. The front end (Fig. 2) of such a machine would be suitable for studies of s-channel production of a light Higgs boson.

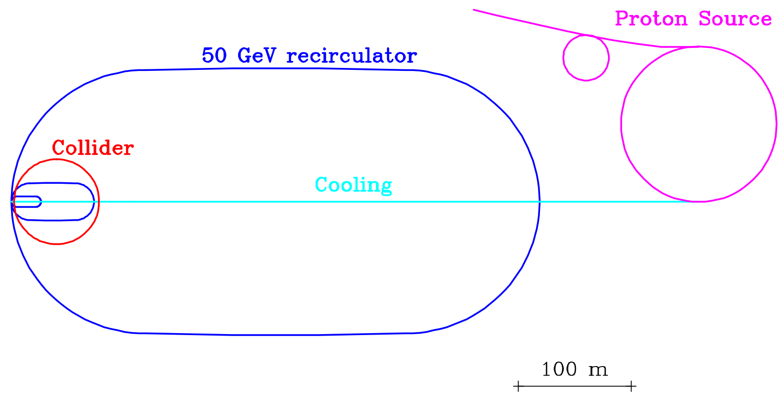

Figure 2: Plan of a 100-GeV CoM Muon Collider, as an example of a first muon collider to study s-channel light-Higgs production.

Of course, muons are unstable with a lifetime of 2.2 μs in the muon's rest frame. Therefore, copious quantities of muons are required to maintain good luminosity. For this, the muons will be collected over a relatively large volume of phase space, which must quickly be reduced by a cooling process. As muons have little interaction with matter, the cooling can be accomplished by a technique not suitable for other particles, namely ionization cooling [3, 4]. In this process, muons lose their transverse and longitudinal momentum during passage through bulk matter, after which only longitudinal momentum is restored via acceleration in rf cavities, as sketched in Fig. 3.

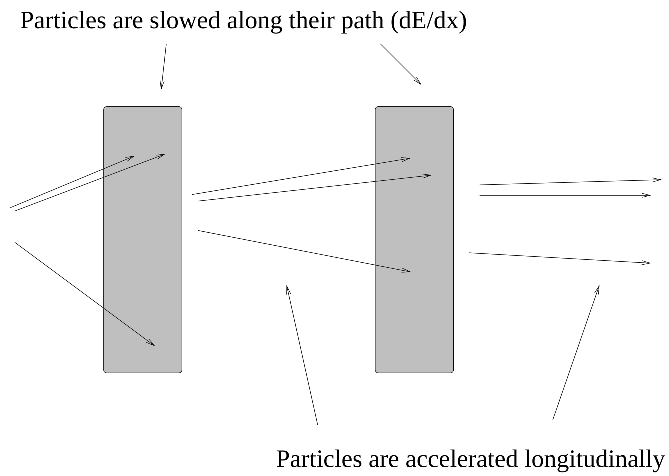

Figure 3: The concept of ionization cooling.

The muon-decay products are electrons and neutrinos, so a muon collider would be the premier source of future neutrino beams. Indeed, some care as to personnel safety from neutrino-induced radiation will be required in multi-TeV muon colliders.

A collaboration [5] of over 100 members[2] has been active for several years in exploring the concept of a muon collider via analytic studies and computer simulation. This effort is summarized in refs. [1, 2] and references therein. A key conclusion is that the concepts of a muon collider should be validated by a program of research and development in two areas:

- Ionization cooling;
- Targetry.

A proposal for an R&D program on ionization cooling [6] has recently been submitted to Fermilab. The present document proposes a companion program for targetry issues: the production of pions by protons hitting a target, and the subsequent capture and decay of the pions to produce the initial muon beam.

1.2 A Targetry Scenario for a Muon Collider

This subsection first discusses the choice of target technology, optimization of the target geometry, and then describes design studies for the pion capture and phase-rotation channel.

Figure 4 gives an overview of the configuration for production of pions by a proton beam impinging on a long, thin target, followed by capture of low-momentum, forward pions in a channel of solenoid magnets with rf cavities to compress the bunch energy while letting the bunch length grow: thus rotating the bunch in phase space.

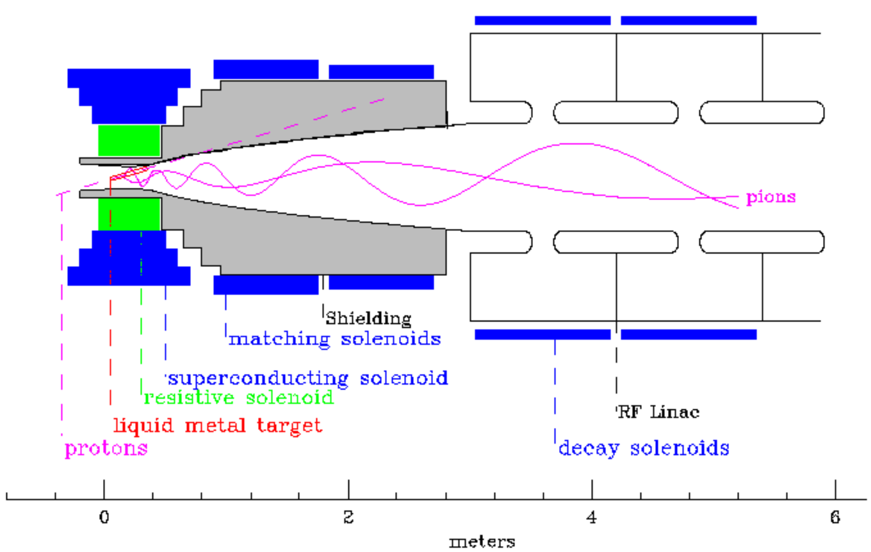

Figure 4: Schematic view of pion production, capture and initial phase rotation: A pulse of 16-30 GeV protons is incident on a skewed target inside a high-field solenoid magnet followed by a decay and phase-rotation channel.

[2]Spokesperson: R.B. Palmer.

1.2.1 Pion production

To achieve the present design luminosity of 7×10^{34} cm^{-2}s^{-1} for a 3-TeV CoM muon collider (or 10^{31} cm^{-2}s^{-1} at 100-GeV CoM), 2×10^{12} (or 4×10^{12} at 100-GeV CoM) muons of each sign must be delivered to the collider ring in each pulse at 15 pps. We estimate that a muon has a probability of only 1/4 of surviving the processes of cooling and acceleration, due to losses in beam apertures or by decay. Thus, 0.8×10^{13} muons (1.6×10^{13} at 100 GeV) must exit the phase-rotation channel each pulse. For pulses of 2.5×10^{13} protons (5×10^{13} for 100 GeV), this requires 0.3 muons per initial proton. And since the efficiency of the phase-rotation channel is about 1/2, this is equivalent to a capture of about 0.6 pions per proton: a very high efficiency.

The pions are produced in the interaction of the proton beam with the primary target. Extensive simulations have been performed for pion production from 8-30-GeV proton beams on different target materials in a high-field solenoid [2, 7, 8, 9, 10]. Three different Monte Carlo codes [11, 12, 13, 14] predict similar pion yields despite significant differences in their physics models. The Collaboration is involved in an AGS experiment [15] to measure the yield of very low momentum pions, which will validate the codes in the critical kinematic region.

The pion yield is greater for relatively high-Z materials, and for these, the pion yield is maximal for longitudinal momenta of the same order as the average transverse momentum ($\approx$ 200 MeV/c). Targets of varying composition ($6 < Z < 82$), radii (0.2-3 cm) and thicknesses (0.5-3 nuclear interaction lengths (λ_I)) have been explored. For a fixed number of interaction lengths, the pion yield per proton rises almost linearly with proton energy [10], and hence almost proportional to the energy deposited in the target. The yield is higher for medium and high-Z target materials, with a noticeable gain at $Z > 26$ for 30-GeV proton beams, but with only a minor effect for $E \leq 16$ GeV, as shown in Fig. 5a).

1.2.2 Target

The target should be 2-3 interaction lengths long to maximize pion production. A high-density material is favored to minimize the size and cost of the capture solenoid magnet. Target radii larger than about 1 cm lead to lower pion rates due to reabsorption, while smaller diameter targets reduce the added production from secondary interactions. Tilting the target by 100-150 mrad minimizes loss of pions by absorption in the target after one turn on their helical trajectory. Another advantage of the tilted target geometry is that the high-energy and neutral components of the shower can be absorbed in a water-cooled beam dump to the side of the focused beam (see Fig. 4).

About 30 kJ of energy is deposited in the target by each proton pulse (10% of the beam energy). Hence, the target absorbs 400 kW of power at the 15-Hz pulse rate. Cooling of the target via contact with a thermal bath would lead to unacceptable absorption of pions, and radiative cooling is inadequate for such high power in a compact target. Therefore, the target must move so as to carry the energy deposited by the proton beam to a heat exchanger outside the solenoid channel.

Both moving-solid-metal and flowing-liquid targets have been considered, with the latter as the currently preferred solution. A liquid is relatively easy to move, easy to cool, can

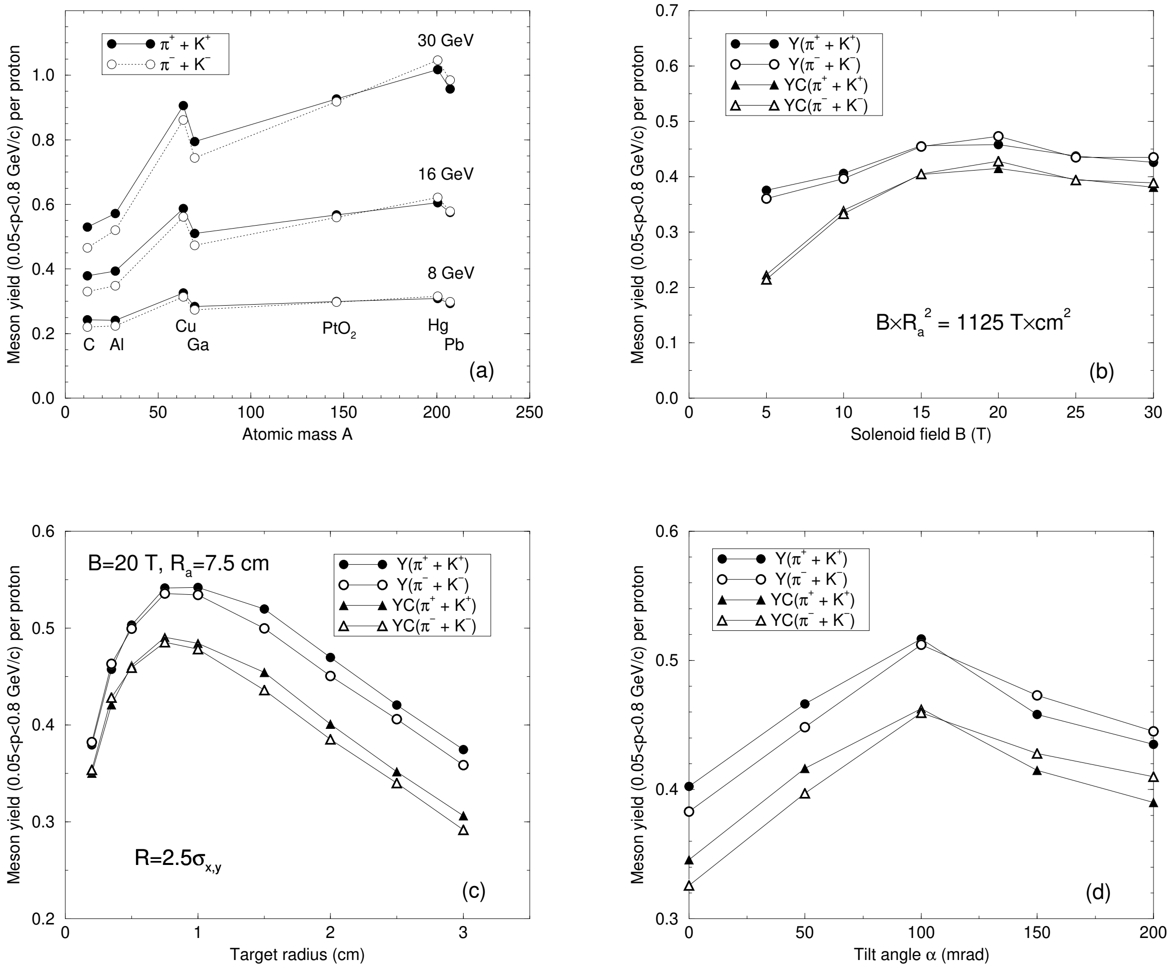

Figure 5: a) Meson yield ($\pi + K$) from a 1.5-λ_I, 1-cm-radius target irradiated with 8, 16 and 30-GeV proton beams as a function of target atomic mass; b) Meson yield from a 3-λ_I, 1-cm-radius gallium target tilted at angle 150 mrad in a 16-GeV proton beam *vs.* solenoid field for a fixed adiabatic invariant BR_a^2; c) Meson yield as a function of target radius; d) Meson yield *vs.* tilt angle between the axis of the capture solenoid and the proton beam. The target is aligned along the beam. The curves labeled YC show mesons that are transported into the decay channel.

be readily removed and replaced, and is the preferred target material for most spallation neutron sources under study. A liquid flowing in a pipe was considered, but experience at CERN [16] and Novosibirsk [17] indicates that shock damage to the pipe is a serious problem. An open liquid jet is thus proposed.

A jet of liquid mercury has been demonstrated [18] (see Figs. 6 and 7) but not exposed to a beam. For our application, safety and other considerations favor the use of a low-melting-point lead alloy rather than mercury. Gallium alloys, though with lower density, are also being considered.

It is expected that the jet will disperse after being struck by the beam. The target station must survive damage resulting from the violence in this dispersion. This consideration will determine the minimum beam, and thus jet, radius.

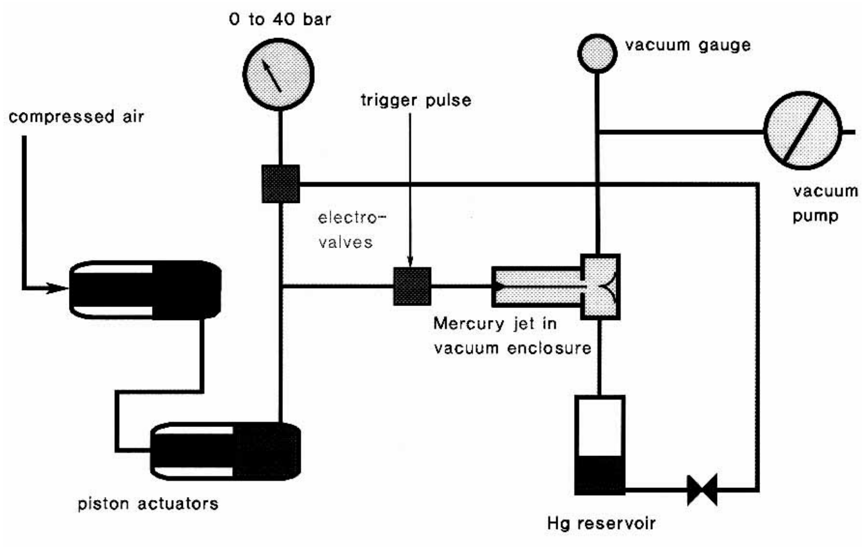

Figure 6: Block diagram of a mercury jet.

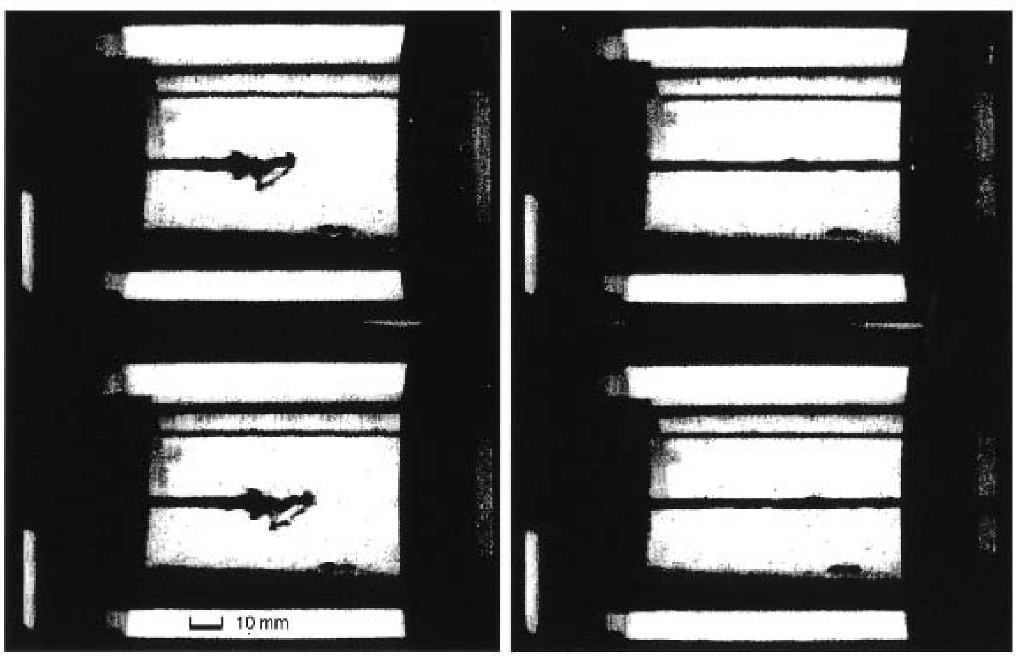

High-speed photographs of mercury jet target for CERN-PS-AA. (laboratory test)
4,000 frames per second, Jet speed: 20 ms^{-1}, diameter: 3 mm, Reynold's Number: >100,000
A. Poncet

Figure 7: Photographs of a 3-mm-diameter mercury jet.

For a conducting liquid jet in a strong magnetic field, as proposed, strong eddy currents will be induced in the jet, causing reaction forces that may disrupt its flow [19, 20]. The forces induced are proportional to the square of the jet radius, and set a maximum for this radius of order 5-10 mm. If this maximum is smaller than the minimum radius set by shock considerations, then multiple smaller beams and jets could be used; *e.g.*, four jets of 5 mm radius with four beams with 2.5 10^{13} protons per bunch. Alternatives include targets made from insulating materials such as liquid PtO_2 or Re_2O_3), slurries (*e.g.*, Pt in water), or powders [21].

A moving-solid-metal target is not the current baseline solution, but is a serious possibility. In this case [22], the target could consist of a long flat band or hoop of copper-nickel that moves along its length (as in a band saw). The band would be many meters in length, would be cooled by gas jets away from the target area, and would be supported and moved by rollers, as shown in Fig. 8.

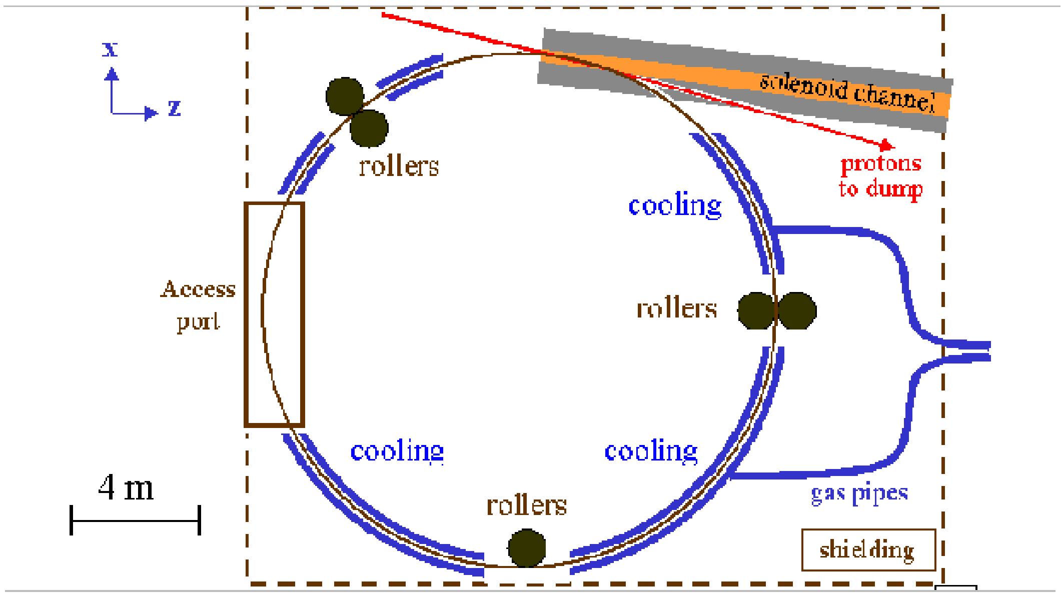

Figure 8: Alternative concept of a solid metal target in the form of a rotating Cu-Ni band.

1.2.3 Capture

In order to capture all pions with transverse momenta $P_\perp$ less than their typical values of 200 MeV/c, the product of the capture solenoid field B and its radius R_a must be greater than 1.33 T-m. The use of a high field and small radius is preferred to minimize the corresponding transverse emittance, which is proportional to BR^2: for a fixed transverse momentum capture, this emittance is thus proportional to R. A field of 20 T and 7.5 cm radius was chosen on the basis of simulations described below. This gives $BR = 1.5$ T-m, $BR^2 = 0.1125$ T-m^2 and a maximum transverse-momentum capture of $P_\perp = 225$ MeV/c.

A preliminary design [23] of the capture solenoid has an inner 6-T, 4-MW, water-cooled, hollow-conductor magnet with an inside diameter of 24 cm and an outside diameter of 60 cm. There is space for a 4-cm-thick, water-cooled, heavy-metal shield inside the coil. The outer superconducting magnet has three coils, with inside diameters of 60 to 80 cm. It generates an additional 14 T of field at the target and provides the required tapered field to match into the decay channel. Such an hybrid solenoid has parameters compatible with those of existing magnets [24].

The 20-T capture solenoid is matched via a transfer solenoid [7] into a decay channel consisting of a system of superconducting solenoids with the same adiabatic invariant $BR^2 \propto RP_{\perp}$. Thus, for a 1.25-T decay channel, B drops by a factor of 1/16 between the target and decay channel, R and $P_{\perp}$ change by factors of 4 and 1/4, respectively. This permits improved acceptance of transverse momentum within the decay channel, at the cost of an increased spread in longitudinal momentum.

Detailed results of a simulation of pion production and capture are shown in Fig. 5.

The curves labeled YC in Fig. 5b) show the yield of pions that are both captured in the high-field solenoid and transported into the decay channel as a function of field in the capture solenoid, with the radius of the capture solenoid adjusted to maintain the same BR_a^2 as in the decay channel. The optimum field is 20 T in the capture solenoid.

Figure 5c) shows that pion production *vs.* target radius has a maximum near $r = 0.85$ cm. This is the result of the competition between secondary production and tertiary absorption, both of which increase with target radius.

If the axis of the target is coincident with that of the solenoid field, then there is a relatively high probability that pions re-enter the target after one cycle on their helical trajectory and are lost due to nuclear interactions. When the target and proton beam are set at an angle of 100-150 mrad with respect to the field axis, the probability for such pion interactions at the target is reduced, and the overall production rate increased by 60%, as shown in Fig. 5d).

In sum, the simulations indicate that a 20-T solenoid of 16-cm inside diameter surrounding a tilted target will capture about half of all produced pions. With target efficiency included, about 0.6 pions per proton will enter the pion decay channel [10].

1.2.4 Phase-Rotation Linac

The pions, and the muons into which they decay, have an energy spread with an rms value of approximately 100% and a peak value at about 200 MeV/c. It would be difficult to handle such a wide spread in any subsequent system. A linac is thus introduced along the decay channel, with frequencies and phases chosen to deaccelerate the fast particles and accelerate the slow ones; *i.e.*, to phase rotate the muon bunch.

Several studies have been made of the design of this system, using differing ranges of rf frequency, delivering different final muon momenta, and differing final bunch lengths. In all cases, efficiencies of close to 0.3 muons per proton are obtained. Until the early stages of the ionization cooling have been designed, it is not yet possible to choose between them.

Independent of the above choices is the question of the location of the focusing solenoid coils and rf cavity design. The closer the first rf cavity is to the target, the less the muon bunch lengthens due to the variation in velocity of the pions.

We discuss here only the case where muons are captured at a mean kinetic energy of 130 MeV. See ref. [1] for an example of capture at a higher energy. Table 1 gives parameters of the linacs used. The frequencies vary between 30 and 60 MHz, and the overall length is 42 m.

Monte Carlo simulations [2], with the program MUONMC [25], were done using pion production calculated by ARC [11] for a copper target of 1 cm radius at an angle of 150 mrad. A uniform solenoidal field was assumed in the phase rotation, and the rf was approximated by a series of kicks.

Table 1: Parameters of Phase-Rotation Linacs

Linac	Length (m)	Frequency (MHz)	Gradient (MeV/m)
1	3	60	5
2	29	30	4
3	5	60	4
4	5	37	4

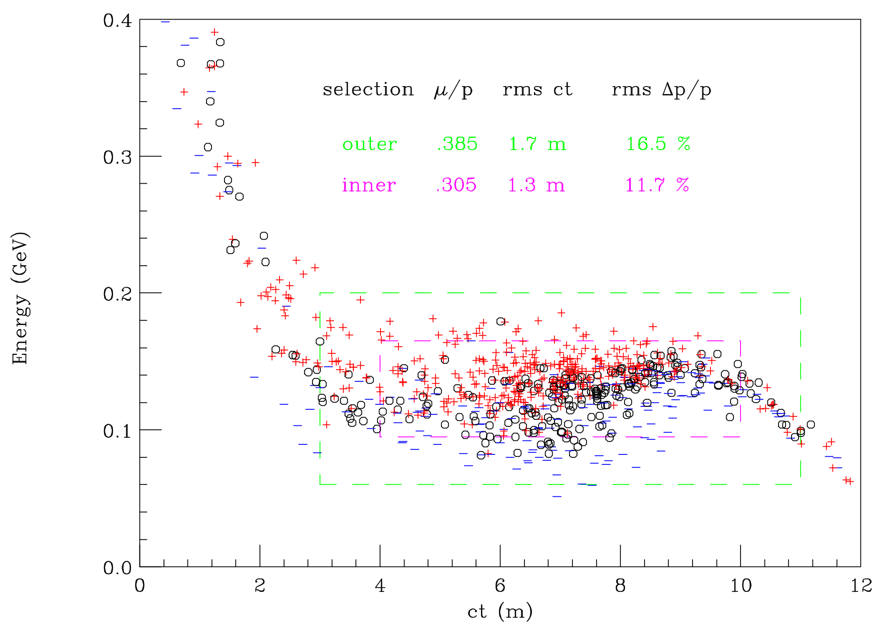

Figure 9: Energy *vs.* ct of μ's at end of the phase-rotation channel. The symbols +, o and − denote muons with polarization $P > \frac{1}{3}$, $-\frac{1}{3} < P < \frac{1}{3}$ and $P < -\frac{1}{3}$, respectively. Without energy selection, the average polarization of the muons is 20%.

Fig. 9 shows the energy *vs.* ct at the end of the decay and phase-rotation channel. A loose final-bunch selection was defined with an energy 130 ± 70 MeV and bunch ct from 3 to 11 m. With this selection, the rms energy spread is 16.5%, the rms ct is 1.7 m, and there are 0.385 muons per incident proton. A tighter selection with an energy 130 ±+ 35 MeV and bunch ct from 4 to 10 m gave an rms energy spread of 11.7%, rms ct of 1.3 m, and contained 0.305 muons per incident proton.

1.2.5 Use of Both Signs

Protons on the target produce pions of both signs, and a solenoid will capture both, but the subsequent phase-rotation rf systems will have opposite effects on opposite charges within the same bunch. The baseline solution is to use two proton bunches, separated in time by an odd number of rf half cycles.

A second possibility would be to separate the charges into two channels, and phase rotate them separately. However, the separation, probably using a bent solenoid, is not simple and would not be fully efficient. Whether a gain in overall efficiency could be achieved is not yet known.

1.2.6 Solenoids and RF

Pion capture using higher frequencies appears to be less efficient, and most studies now use frequencies down to 30 MHz. Such cavities, when conventionally designed, are very large (about 6.6 m diameter). In the Snowmass study [27], a reentrant design reduced this diameter to 2.5 m, but this is still large, and it was first assumed that 5-T focusing solenoids would, for economic reasons, be placed within the irises of the cavities (see Fig. 10).

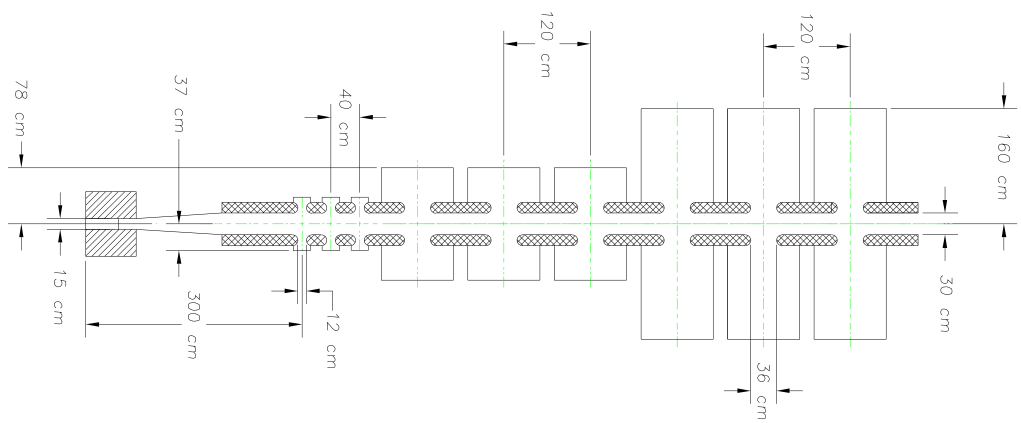

Figure 10: Schematic of capture and phase rotation using rf cavities with superconducting solenoids (hatched) inside the irises. Only three sections each are shown for cavities operating at 90, 50, and 30 MHz.

However, a study [28] of transmission down a realistic system of iris-located coils revealed betatron resonant excitation from the magnetic-field periodicities, leading to significant particle loss. This was reduced by the use of more complicated coil shapes [27], smaller gaps, and shorter cavities, but remained a problem.

An alternative is to place continuous focusing coils outside the cavities (as shown in Fig. 4). In this case cost will be minimized with lower magnetic fields (1.25-2.5 T) and correspondingly larger decay channel radii (21-30 cm). Simulations are underway to determine the optimal solution.

1.2.7 Muon Polarization

Polarization of the muon beams presents a significant physics advantage over the unpolarized case, since signal and background of electroweak processes usually come predominantly from different polarization states.

In the center of mass of a decaying pion, the outgoing muon is fully polarized ($P = -1$ for μ^+ and $+1$ for μ^-). In the lab system the polarization depends on the decay angle θ_d and initial pion energy [29, 30]. For pion kinetic energy larger than the pion mass, the average polarization is about 20%, and if nothing else is done, the polarization of the captured muons after the phase-rotation system is approximately this value.

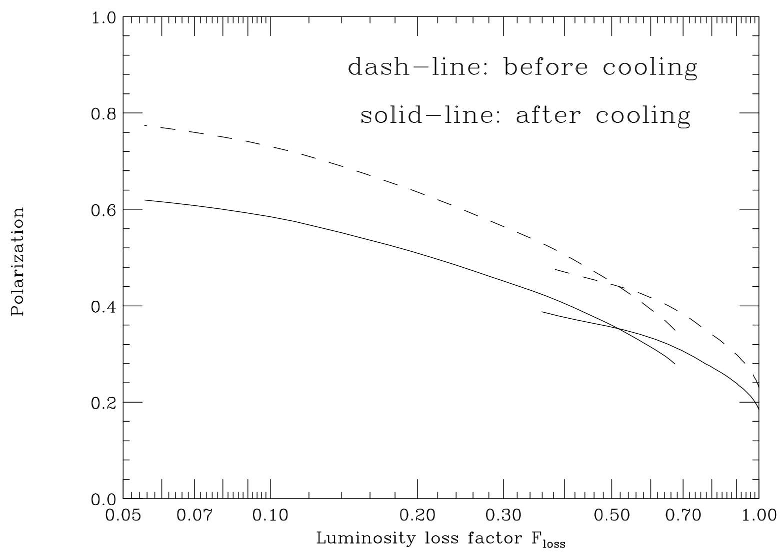

Figure 11: Polarization *vs.* fraction $F_{\rm loss}$ of μ's accepted.

If higher polarization is required, some selection of muons from forward pion decays ($\cos\theta_d \to 1$) is required. Figure 9 shows the polarization of the phase-rotated muons. The polarization {P> $\frac{1}{3}$, $-\frac{1}{3} < P < \frac{1}{3}$, and P< $-\frac{1}{3}$} is marked by the symbols +, **o** and − respectively. If a selection is made on the minimum energy of the muons, then greater polarization is obtained. The tighter the cut, the higher the polarization, but the less the fraction $F_{\rm loss}$ of muons that iremain. Figure 11 gives the results of a Monte Carlo study.

If this selection is made on both beams, and if the proton-bunch intensity is maintained, then each muon bunch is reduced by the factor $F_{\rm loss}$ and the luminosity would fall by $F_{\rm loss}^2$. But if, instead, proton bunches are merged so as to obtain half as many bunches with twice the intensity, then the muon-bunch intensity is maintained and the luminosity (and repetition rate) falls only as $F_{\rm loss}$.

The luminosity could be maintained at the full unpolarized value if the proton-source intensity could be increased. Such an increase in proton-source intensity in the unpolarized case might be impractical because of the resultant excessive high-energy-muon beam power, but this restriction does not apply if the increase is used to offset losses in generating polarization.

Thus, the goal of high muon-beam polarization may shift the parameters of the muon collider towards lower repetition rate and higher peak currents at the pion-production target.

1.3 Summary of Critical Targetry Issues

There are four key issues which require laboratory studies before the targetry scenario can be placed on a firm basis:

1. What is the yield of low-energy pions from 16-30-GeV protons on heavy targets?

2. What is the effect of the pressure wave induced in the target by the proton pulse? If the liquid target is dispersed by the beam, do the droplets damage the containment vessel?

3. What is the effect of the magnetic field of the capture solenoid on the motion of the liquid-jet target? Does the magnetic field damp the effects of the beam-induce pressure wave?

4. Can the first rf cavity of the phase-rotation channel operate viably in close proximity to the target?

Of course, detailed simulations are ongoing to answer as many question as possible without additional empirical data.

Question 1 is being addressed by BNL experiment E-910 [15], the status of which is summarized in an Appendix. The present understanding of questions 2-4 is discussed in sec. 2, and the proposed eight-part R&D program to address these questions is presented in sec. 3.

2 Critical Targetry Issues

2.1 Solid or Liquid Target?

The muons of a muon collider will arise from the decay of pions produced in the interaction of some 1.5×10^{15} protons/s on a primary target. If these protons have 16-GeV energy, the beam power is 4 MW. The target will be about 2 interaction lengths long and will absorb about 10% of the beam power, *i.e.*, about 400 kW. The beam repetition rate is 15 Hz, so each beam pulse deposits about 30 kJ of energy in the target.

2.1.1 Cooling the Target

The target is in the form of a cylinder, about 1 cm in radius, 30 cm in length, with a volume of about 100 cm^3. If the target material has density 10 g/cm^3, then the target mass is about 1 kg. Thus the beam-energy deposition in the target averages about 30 J/g. Taking the heat capacity of a typical metal as 0.2 J/(g-°K), the temperature rise of a metallic target is about 150°K per pulse. If the target is not cooled it would melt (if solid) or boil (if liquid) in a few seconds.

However, the goal of collecting the maximal number of muons per proton is not consistent with typical cooling schemes in which the target material is in immediate contact with a large thermal reservoir.

Radiative cooling of the target appears to be implausible. The power radiated by a surface of area A and emissivity ϵ at temperature T is $\epsilon\sigma T^4 A$, where $\sigma = 5.67 \times 10^{-12}$ J/(cm^2(°K)^{4}s) is the Stefan-Boltzmann constant. The emissivities of typical metals are only about 0.2 (in contrast to carbon with $\epsilon \approx 0.8$). The surface area of the target cylinder is about 200 cm^2. If the target could be operated at 2000°K, then the radiated power would be about 3.6 kW, compared to the 400-kW beam load.

Thus, we are led to consider scenarios in which the target is in motion, with any subunit of the target exposed to only one or a few beam pulses before being transported away from the interaction region to be cooled by a remote thermal reservoir. For similar reasons, targets at multimegaWatt neutron spallation sources are expected to be based on flowing liquid metal, usually mercury [31, 32, 33, 34, 35].

2.1.2 Thermal Shock

The simplest option would be use of a flowing liquid metal contained within a static metal pipe [37, 38, 39]. However, when a large pulse of energy is deposited in a material in a time that is short compared to the transit time of a sound wave (≈ 2 μs/cm) a pressure (stress) wave results [40, 41, 42, 43, 44, 45, 46]. Since the proton pulse for a muon collider is expected to be only about 2 ns long, stress waves will be excited in the target, and consequent damage to the target and adjacent material is a concern.

This issue is often called "thermal shock". However, thermal shock is not, in general, associated with a shock wave of fluid dynamics in which the velocity of part of the fluid exceeds that of sound.

The Initial Pressure Wave If the beam-induced stress exceeds the tensile strength of the target material the latter would fracture.

We present a simplified model to estimate the regime in which a pressure wave will "tear" the target apart, whether solid or liquid (see also Refs. [40, 47]). When an energy density ΔU (per gram) is deposited quickly in the target we first calculate the temperature change ΔT that would occur, assuming no thermal diffusion. Then, we calculate the strain, $\Delta l/l$ corresponding to that ΔT, and evaluate the stress P corresponding to that strain. Tearing is likely to occurs if the stress exceeds the tensile strength. In this model, tearing occurs during the phase of the pressure wave when the material is under tension, *i.e.*, for negative pressure. In liquids, this phenomenon is called cavitation [48, 49, 50].

We suppose that the effective tensile strength of a liquid metal is similar to that of the same metal in solid form. For example, the tensile strength of sea ice is reported as about 8 atm. [51], while that of water can exceed 200 atm. in a static measurement [52] but was measured as 8 atm. by an explosive technique [53] that has much in common with the present concerns; see also [48, 49].

For most metals, the tensile strength (pressure) P is about 0.002 of the modulus of elasticity, E (Young's modulus). Thus,

$$\Delta U = C\Delta T = \frac{C}{\alpha}\frac{\Delta l}{l} = \frac{C}{\alpha}\frac{P}{E} \approx 0.002\frac{C}{\alpha}, \tag{1}$$

where C is the heat capacity, α is the coefficient of thermal expansion, and the approximation holds on setting the stress equal to the tensile strength. If for example, the heat capacity is $C = 0.3$ J/g-°C and $\alpha \approx 2 \times 10^{-5}$/°C, then we expect the target material will tear when $\Delta U \approx 30$ J/g. This is very similar to the expected energy deposition in the muon-collider target. It is, however, somewhat smaller than a semi-empirical value of 200 J/g for the threshold for thermal-shock damage [54].

If the target tears it is possible that the fragments do damage to the surrounding vessel. If all the deposited energy were converted to kinetic energy and the target fragmented completely, then the velocity of the fragments would be $\sqrt{2\Delta U} \approx 8$ m/s for $\Delta U = 30$ J/g. A model of spray velocities in explosions of liquids [53] leads to similar values. Thus, it is encouraging that if, say, a liquid target is dispersed into droplets by the beam, the droplets would do little damage to the surrounding vessel. However, this should be confirmed by experiment.

The Reflected Pressure Wave Even if target parameters are chosen such that the initial pressure wave does not tear the material, there is another concern. When the pressure wave reaches the surface of the target it will be reflected, in general. In the case of a cylindrical target, the reflected wave converges on the axis of the target and will typically result in higher peak pressures than exist in the initial outgoing wave. Hence, there is a serious prospect for localized fracture or vaporization of the target material close to the target axis, whether the cylindrical target is solid or liquid. In the case of a liquid, this is likely to induce localized damage to the target pipe, particularly on the upstream wall.

The destructive effects of pressure waves and cavitation on liquid-metal targets in pipes have been demonstrated at the CERN ISOLDE facility [16, 55] as shown in Figs. 12-13, and also at the Budker Institute [17] as shown in Fig. 14. Practical targets based on liquid metals in pipes requires sufficiently long beam pulses and/or target geometries (*i.e.*, planar) in which imploding pressure waves do not occur. Therefore, liquids in pipes are not consider further for a muon-collider target. Likewise, a moving solid cylindrical target is very problematic at a muon collider.

2.1.3 Muon-Collider Primary-Target Options

The remaining options for the muon-collider target are a free, cylindrical liquid-metal jet or a moving planar solid target, as have been sketched in Figs. 4 and 8. The baseline design to be studied in the proposed R&D program utilizes a free liquid-metal jet. The moving band target is presently considered as the backup option.

2.1.4 Additional Issues for a Solid Target

As well as surviving the thermal-shock of each beam pulse, a solid target must survive the long-term effects of radiation damage. These include embrittlement, swelling and even

Figure 12: Full-scale model of an ISOLDE target consisting of a 2-cm-diameter, 20-cm-long tantalum cylinder containing molten lead.

Figure 13: Photograph of an ISOLDE liquid-lead target that ruptured around the upstream window after a few beam pulses [16].

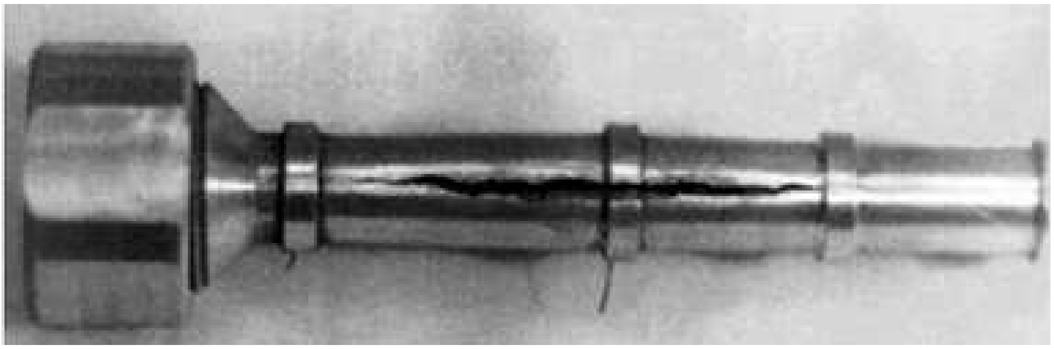

Figure 14: Photograph of a mercury target contained in an aluminum cylinder that ruptured after exposure to a beam that deposited 1 kJ/g per pulse [17].

fracture of the material due to displacement damage and hydrogen/helium production [56]. The immunity of a liquid target to these effects is an argument favor of that option.

The cross section for displacement of a target atom in a 16-30-GeV proton beam is about 10^{-24} m^2. In an operational year of 10^7 s, a beam of 1.5×10^{15} proton/s whose rms radius is nominally 4 mm results in about 300 displacements per atom (dpa) in a nonmoving target.

For a moving solid target, any given atom is exposed to a proton flux that is less than the total by the factor

$$\frac{L\mathrm{int} N_{\mathrm{overlap}}}{L_{\mathrm{total}}}, \tag{2}$$

where L_{int} is the length of the interaction region ($\approx$ 30 cm), L_{total} is the total length of the target material ($\approx$ 30 m, say) and N_{overlap} is the number of adjacent beam pulses that irradiate a given region. That is,

$$N_{\mathrm{overlap}} = \frac{L_{\mathrm{int}} f}{v}, \tag{3}$$

for a target moving with velocity v along the beam whose pulse rate is f Hz. For example, with $v = 1$ m/s and $f = 15$ Hz then $N_{\mathrm{overlap}} = 5$, and each part of the moving target experiences only 5% of the exposure of a nonmoving target, namely about 15 dpa in a year of operation. This corresponds to significant radiation damage, and the viability of a moving solid target needs further investigation.

There is little available evidence as to the mechanical properties of targets after such exposures. A series of studies of solid targets at CERN generally indicated severe mechanical damage to intensely irradiated targets [57, 58, 60, 61, 62], although the damage was due to a combination of single-pulse shock as well as radiation. Nickel targets appear to survive well for energy depositions up to a large fraction of the shock-damage threshold [63].

2.2 Beam-Induced Radioactivity

The high flux of protons into the target will induce some radioactivity no matter what the target consists of. A thorough study of this issue will be needed before a final decision as to the target material is taken.

Especially high levels of activity would arise for targets containing bismuth, due to the sequence:

$$\text{Low-energy neutron} + \text{Bi}_{83}^{209} \to \text{Bi}_{83}^{210} + \gamma, \qquad \text{Bi}_{83}^{210} \to \text{Po}_{84}^{210} + \beta^- \quad \text{(half life = 5 days)}. \quad (4)$$

Po^{210} has a half life of 135 days and decays primarily via a 5.3-MeV α, but has a 0.1% branch to an 803-keV x-ray.

If, say, every beam proton results in one transmutted Bi atom, then the steady-state Po population would be equal to the total flux of protons in 135 days = $135 \times 10^5 \times 10^{15} \approx 10^{22}$ atoms, assuming a proton flux of 10^{15}/s. The number of Po decays per second would be just 10^{15} in the steady state, *i.e.*, about 30,000 Curies.

The α-particles will be almost entirely absorbed in the target, but the 800-keV x-rays present more of a problem. The steady-state strength of the x-rays corresponds to about 30 Curies (assuming each proton results in one Po atom).

However, the resulting polonium would be dissolved in the liquid of the target with very low probability of being in vapor molecules. Hence, the handling of an activated bismuth alloy would be relatively straightforward and little more difficult than for other target materials [64].

2.3 Candidate Liquid Metals

Liquid metals have long been considered and used as coolants for nuclear reactors, and a useful summary of candidate materials has been given by Lyon [65]. Table 2 presents a brief survey of low-melting-temperature metals, and Table 3 list some relevant physical properties of the elements of candidate materials.

We are interested in high-Z, high-density target materials for the most efficient pion production. High electrical resistivity is helpful in reducing the eddy-current problem of a jet entering a magnetic field.

In many ways mercury is an excellent candidate, although its vapors are toxic. Also, it may be preferable to use a material that is solid at room temperature to simplify cleanup of spills. Lead alloys (solder-like materials) are good candidates. Rather low melting temperatures are obtained by alloying with indium, which however wets most solid metals so much as to make it difficult to produce liquid jets. Lead-bismuth alloys have the drawback of relatively high production of polonium when activated by the proton beam. Gallium alloys are nontoxic and can be liquid at room temperature, so the resulting ease of handling indicates their use in the initial stages of the R&D program. The relatively low atomic number, low density and low resistivity of gallium is somewhat undesirable for use in the final target.

2.3.1 Mercury

Studies of materials issues for use of mercury as a proton target include Refs. [42, 66, 67, 68]. The tensile strength of liquid mercury has been studied by Briggs [52, 69].

2.3.2 Lead Alloys

A lead alloy of particular interest is eutectic lead-bismuth, 45% Pb by weight with a melting point of 126°C (255°F). Other interesting low-melting allows of lead and/or bismuth are

Table 2: Survey of low-melting-temperature metals [65].

Approximate melting point, °C	Approximate composition, wt %
185	48 bismuth, 52 thallium (eutectic)
180	38 lead, 62 tin (eutectic)
140	60 bismuth, 40 cadmium (eutectic)
140	58 bismuth, 42 tin (eutectic)
130	56 bismuth, 40 tin, 4 zinc (eutectic)
125	44.5 bismuth, 55.5 lead (eutectic)
120	25 cadmium, 75 indium (eutectic)
117	48 tin, 52 indium (eutectic)
105	48 bismuth, 28.5 lead, 14.5 tin, 9.0 antimony (matrix alloy)
93	50 bismuth, 25 lead, 25 tin
91.5	51.6 bismuth, 40.2 lead, 8.2 cadmium (eutectic)
71.7-69.7	50 bismuth, 25 lead, 12.5 tin, 12.5 cadmium (Wood's metal)
70	33 bismuth, 67 indium (eutectic)
70	50 bismuth, 26.7 lead, 13.3 tin, 10 cadmium (eutectic)
60.5	32.5 bismuth, 16.5 tin, 51 indium
58.2	49.5 bismuth, 17.6 lead, 11.6 tin, 21.3 indium
46.5	40.63 bismuth, 22.11 lead, 10.65 tin, 8.2 cadmium, 18.1 indium
33	32 potassium, 68 rubidium (eutectic)
17	12 tin, 6 zinc, 82 gallium (eutectic)
10.8	12.5 tin, 17.6 indium, 69.8 gallium (eutectic)
10.7	16 tin, 21.5 indium, 62.5 gallium (eutectic)
−8	8 sodium, 92 rubidium (eutectic)
−11	22 sodium, 78 potassium (eutectic)
−30	5 sodium, 95 cesium (eutectic)
−40	87 cesium, 13 rubidium (eutectic)
−48	23 potassium, 77 cesium (eutectic)

made by adding cadmium, indium or tin. Some quaternary and quinternary alloys have extremely low melting temperature, such as alloys 117 and 136 (designated by their melting temperatures in °F). Table 4 gives a summary of physical properties of several commercial lead alloys.

We have verified that the resistivities of liquid-lead alloys are very similar to those of the corresponding solid, as listed in Table 4 [19].

An extensive literature exists on materials handling issues for applications of lead alloys at nuclear reactors [70, 71, 72, 73, 74, 75].

Table 3: Properties of some candidate elements for primary targets.

Element	Z	Density (g/cm^3)	Melting Temp. (°C)	Boiling Temp. (°C)	Heat Cap. (J/g-°C)	Heat of Vapor. (J/g)	Thermal Cond. (W/cm-°C)	Resist. ($\mu\Omega$-cm)	Thermal Exp. (10^{-5}/°C)
Copper	29	8.96	1083	2336	0.39	4725	0.39	1.7	1.7
Zinc	30	6.6	420	906	0.50	1733	0.25	33	3.0
Gallium	31	5.9	30	2403	0.37	3712	0.48	26	12
Indium	49	7.3	156	2073	0.23	2016	0.82	29	3.2
Tin	50	6.7	232	2603	0.23	2487	0.67	48	2.2
Mercury	80	13.5	-39	357	0.14	295	0.083	98	6.0
Lead	82	11.35	327	1750	0.13	858	0.35	95	2.9
Bismuth	83	9.7	271	1610	0.12	501	0.079	129	1.3

2.3.3 Gallium and Gallium Alloys

Some information on liquid gallium alloys can be found at
`http://www.indium.com/liquidalloys.html`

The eutectic Ga-Sn alloy is particularly convenient as it is a liquid at room temperature. It is easy to prepare by dissolving tin wire (but not powder) is liquid gallium at 40-50°C. The binary phase diagram for Ga-Sn is shown in Fig. 15.

Liquid gallium has a viscosity of 1.6 cp/g-cm^3, only slightly highly than that of water. The temperature dependence of the resistivity of gallium has been studied in detail [77]. Liquid gallium has been used as a coolant for silicon crystals at synchrotron light sources [78, 79].

2.4 Jet Velocity

To be useful as a target, a pulsed liquid jet must have a minimum velocity so that each pulse is sufficiently distinct from the others, and so that the jet is reasonably straight. The minimum velocity for a conductive jet to enter a strong magnetic field is considered in sec. 2.5.

2.4.1 Effect of 15-Hz Repetition Rate

We consider the use of a pulsed jet, leading to a series of cylinders of liquid, each of length l, radius r, that move with velocity v. The frequency of the pulse is f, nominally 15 Hz.

If the material from one pulse is not to overlap that of the next, then the jet velocity

Table 4: Lead Alloy Specifications from Belmont Metals. See also http://www.indium.com/fusiblealloys.html

Th: Kirk McDonald

Bob $96.80 $10/30

Belmont METALS INC.
330 Belmont Avenue, Brooklyn, New York 11207
(718)-342-4900 • TWX 710-584-2296 • FAX 718-342-0175

SHEET

$51.35LB $13.25

$54.95

BELMONT LOW MELTING ALLOYS - Used as Production Aids

	EUTECTIC ALLOYS					NON EUTECTIC ALLOYS		
PHYSICAL PROPERTIES & NOMINAL COMPOSITION	BELMONT ALLOY 2451	BELMONT ALLOY 2491	BELMONT ALLOY 2505	BELMONT ALLOY 2562	BELMONT ALLOY 2581	BELMONT ALLOY 2431	BELMONT ALLOY 2481	BELMONT ALLOY 2405
Melting Temperature (°F.)	~~117~~	~~136~~	~~158~~	~~255~~	~~281~~	(No definite melting point, see yield temp.)		
Range (°F.)	117-117	136-136	158-158	255-255	281-281	160-190	218-440	281-338
Yield Temp. (°F.)	117	136	158	255	281	162.5	240	302
Weight Lb./In.³	.32	.31	.339	.380	.315	.341	.343	.296
Specific Gravity 20°C	8.9	8.8	9.4	10.3	8.7	9.4	9.5	8.2
Tensile Lb./In.²	5400	6300	5990	6400	8000	5400	13000	8000
*Elongation in 2" Slow Loading %	1.5	50	200	60-70	200*	220*	Less than 1%	200*
Brinell Hardness #	12	14	9.2	10.2	22	9	19	22
*Specific Heat Liquid	.035	.032	.040	.042	.045	.040	.04	.047
*Specific Heat Solid	.035	.032	.040	.03+	.045	.040	.045	.047
*Latent Heat — Fusion Btu./LB.	6	8	14	7.2	20	10		22
*Coefficient of Thermal Expansion	.000025/°C.	.000023/°C.	.000022/°C.	.000021/°C.	.000015/°C.	.000024/°C.	.000022/°C.	.000015/°C.
Thermal Conductivity (Solid) Cal/Cm²/°C/Sec .94 = Copper	—	—	*.045	*.04	*.05	*.05	—	*.09
Conductivity (Electrical) Compared with Pure Copper	3.34%	2.43%	4.17%	1.75%	5.00%	4.27%	2.57%	7.77%
Resistivity, OHMS based on volume standard (Meter, MM²)	.5180	.7081	.4135	.8825	.3445	.4037	.6696	.2219
*Maximum Load — 30 Seconds Lb. — In.²			10000	8000	15000	9000	16000	15000
*Maximum Load — 5 Minutes Lb. — In.²			4000	4000	9000	3800	10000	9500
*Safe Load — Sustained Lb. — In.²			300	300	500	300	300	500
Volume Change (Liquid to Solid)	—1.4%	—1.35%	—1.7%	—1.5%	+0.77%	*—2.0%	—1.5%	*+0.5%
Volume Change (Linear growth after solidification.)	Less Than 0.05%	Less Than 0.05%	0.6%	0.3%	0.05%	0.3%	0.5%	*0%
GROWTH/SHRINKAGE CHARACTERISTICS TIME AFTER CASTING	FIGURES INDICATED ARE IN INCHES PER INCH AS DETERMINED FROM CUMULATIVE GROWTH MEASURED AS THE DIFFERENCE IN LENGTH BETWEEN MOLD AND TEST BAR DIMENSIONS IN A TEST BAR ½" x ½" x 10".							
2 Minutes	+.0005	+.0003	+.0025	—.0008	+.0007	—.0004	+.0008	—.0001
6 Minutes	+.0002	+.0002	+.0027	—.0011	+.0007	—.0007	+.0014	—.0001
30 Minutes	.0000	+.0001	+.0045	—.0010	+.0006	—.0009	+.0047	—.0001
1 Hour	—.0001	.0000	+.0051	—.0008	+.0006	.0000	+.0048	—.0001
2 Hours	—.0002	—.0001	+.0051	—.0004	+.0006	+.0016	+.0048	—.0001
5 Hours	—.0002	—.0002	+.0051	.0000	+.0005	+.0018	+.0049	—.0001
7 Hours	—.0002	—.0002	+.0051	+.0001	+.0005	+.0019	+.0050	—.0001
10 Hours	—.0002	—.0002	+.0051	+.0003	+.0005	+.0019	+.0050	—.0001
24 Hours	—.0002	—.0002	+.0051	+.0008	+.0005	+.0022	+.0051	—.0001
96 Hours	—.0002	—.0002	+.0053	+.0015	+.0005	+.0025	+.0055	—.0001
200 Hours	—.0002	—.0002	+.0055	+.0019	+.0005	+.0025	+.0058	—.0001
500 Hours	—.0002	—.0002	+.0057	+.0022	+.0005	+.0025	+.0061	—.0001
Compositions (%): Bismuth	44.7	49.0	50.0	55.5	58.0	42.5	48.0	40.0
Lead	22.6	18.0	26.7	44.5		37.7	28.5	
Tin	8.3	12.0	13.3		42.0	11.3	14.5	60.0
Cadmium	5.3		10.0			8.5		
Other	Indium 19.1	Indium 21.0					Antimony 9.0	

* APPROXIMATE VALUES

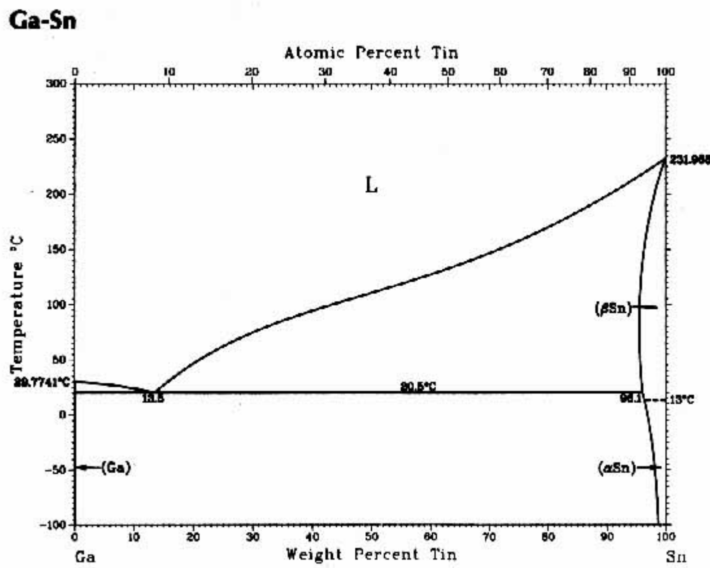

Figure 15: Ga-Sn phase diagram. Minimum melting temperature = 20.5°C [76].

must obey

$$v > fl. \tag{5}$$

For example, the length of each pulse should be about two nuclear interaction lengths, or about 30 cm for a dense, high-Z material. Then with $f = 15$ Hz, we need $v > 4.5$ m/s.

The jet velocity will have to be several times this to create gaps between adjacent pulses so that the proton beam interacts only with a single jet pulse.

2.4.2 Effect of Gravity

The trajectory of the jet will be a parabolic arc due to the acceleration of gravity. If the jet velocity is too low, the curvature of the jet will be large, and the proton beam would not be able to intersect the jet pulse over its whole length.

The ends of the jet are displaced downward from the ideal straight trajectory by amount

$$\Delta y = \frac{gt^2}{2} = \frac{gl^2}{8v^2}, \tag{6}$$

noting that the time for the center of the jet to reach its end is $t = l/2v$. Hence, to have offset Δy between center and ends to the jet, we need

$$v = \sqrt{\frac{gl^2}{8\Delta y}}. \tag{7}$$

For example, with $l = 30$ cm, and $\Delta y = 1/8$ cm as might be desired for a jet of radius 1 cm, we find $v \approx 1000$ cm/s $= 10$ m/s.

Thus the effects of pulse frequency and of gravitational curvature both require the jet velocity to be at least 10 m/s.

2.4.3 Jet Velocity *vs.* Pressure

Suppose the liquid metal is stored in a tank of area A perpendicular to the flow, and the pressure is P above atmospheric. A valve lets a jet of liquid escape through an aperture of area $a \ll A$.

Then Bernoulli's equation tells us that the flow velocity v out the aperture obeys

$$\frac{1}{2}\rho v^2 = P + \frac{1}{2}\rho V^2, \tag{8}$$

where ρ is the density of the liquid and V is the velocity of the liquid surface of area A in the tank. The equation of continuity for an incompressible liquid tells us that $av = AV$, so that

$$v = \sqrt{\frac{2P}{\rho(1-(a/A)^2)}} \approx \sqrt{\frac{2P}{\rho}}. \tag{9}$$

For example, Bi-Pb alloys have density $\rho \approx 10$ g/cm^3, so the jet velocity would be

$$v[\mathrm{m/s}] \approx \sqrt{20P[\mathrm{atm.}]}. \tag{10}$$

Thus, to reach $v = 4.5$ m/s would require 1 atm. overpressure in the storage tank, but 20 atm. would be required to reach 20 m/s.

2.5 The Interaction of a Liquid-Metal Jet with a Magnetic Field

If a jet of liquid metal enters the solenoid magnet surrounding the target area it will be repelled according to Lenz' law. The effect is due to the Lorentz force on the eddy currents induced in the moving metal. In an extreme case the jet would not reach the center of the solenoid.

Here we present simplified analytic estimates of the effects of eddy currents, and reach the tentative conclusion that they would visibly alter the trajectory of the liquid-metal jet, but would not prevent the jet from functioning as a target. However, there appears to be little safety margin, and only laboratory experiments will confirm that the proposed liquid-metal jet is viable.

Additional details of the analytic arguments can be found in Refs. [19, 20, 80].

It is useful to establish numerical values for some relevant parameters of our system as a qualitative guide to its magnetohydrodynamic behavior.

First, we note that the problem of a moving conductor in a static magnetic field is equivalent to a moving field that encounters a conductor initially at rest. Thus, the electric field $\mathbf{E}'$ in the frame of the conductor is related to the electric and magnetic fields $\mathbf{E}$ and $\mathbf{B}$ in the lab frame by

$$\mathbf{E}' = \mathbf{E} + \mathbf{v} \times \mathbf{B}, \tag{11}$$

where $\mathbf{v}$ is the laboratory velocity of the conductor ($v \ll c$), and we use MKSA units.

Next, we recall that the penetration of a time-dependent magnetic field into a conductor is governed by a diffusion equation. Assuming $v \ll c$ and reasonably good conductivity σ, we may neglect the displacement current,and the basic electromagnetic equations are

$$\nabla \times \mathbf{E} = -\frac{\partial \mathbf{B}}{\partial t}, \qquad \nabla \times \mathbf{B} = \mu_0 \mathbf{j}, \qquad \text{and} \qquad \mathbf{j} = \sigma \mathbf{E}' = \sigma(\mathbf{E} + \mathbf{v} \times \mathbf{B}), \tag{12}$$

where $\mathbf{j}$ is the current density. On eliminating $\mathbf{j}$ and $\mathbf{E}$ we find that

$$\frac{\partial \mathbf{B}}{\partial t} = \frac{\nabla^2 \mathbf{B}}{\mu_0 \sigma} + \nabla \times (\mathbf{v} \times \mathbf{B}). \tag{13}$$

With the neglect of the second term (justified for low velocity), we find the desired diffusion equation. Thus, the characteristic time for diffusion of the magnetic field into a long conducting cylinder of radius r is

$$\tau = \mu_0 \sigma r^2. \tag{14}$$

The low-melting temperature alloys in Table 4 all have relatively low conductivity. In particular, alloy 255 has conductivity only 2% that of copper (resistivity = 1.67 $\mu\Omega$-cm), *i.e.*, about 10^6 MKSA units. Hence, for a cylinder of radius 1 cm the diffusion time is

$$\tau \approx 4\pi \times 10^{-7} \cdot 10^6 (10^{-2})^2 \approx 10^{-4} \text{ sec.} \tag{15}$$

Another characteristic time in our problem is that over which the external magnetic field varies appreciably. For a jet of velocity v that enters a solenoid of diameter D, this time is D/v. The ratio of the diffusion time to time D/v is called the magnetic Reynold's number:

$$\mathcal{R} = \frac{\tau v}{D}. \tag{16}$$

For $\mathcal{R} \ll 1$ the external magnetic field penetrates the conductor, but for $\mathcal{R}1$ it does not.

Anticipating a jet velocity of order 10 m/s and a solenoid of diameter $D \approx 0.3$ m, we have $D/v \approx 0.03$ s, and the magnetic Reynold's number is $\mathcal{R} \approx 0.003$. We conclude that in our problem the diffusion is rapid enough that the external field penetrates the conductor. That is, in an important sense our candidate metals are not 'good' conductors which could exclude the magnetic field from their interior. This is fortunate, as a 'good' conductor could not enter a 20-T magnetic field unless its initial velocity were very high.[3]

The magnetic Reynold's number can be thought of in another way. From the point of view of the conductor, the external magnetic field is time dependent with frequency content up to $\omega \approx v/D$. The skin depth at this frequency is $\delta = \sqrt{2/\mu_0 \omega \sigma} = \sqrt{2D/\mu_0 \sigma v}$. This is to be compared to the radius r of the conductor. Indeed,

$$\frac{r^2}{\delta^2} = \frac{\mu_0 \sigma r^2 v}{2D} = \frac{\mathcal{R}}{2}. \tag{17}$$

In our case, the low value of the magnetic Reynold's number indicates that the conductor is much smaller than the relevant skin depth, and again we expect the external field to penetrate the conductor.

We now give some approximate analyses of the forces on the liquid jet as it enters a solenoid.

[3]To see this, consider a good conductor moving along the z-axis of a solenoid field. Surface current $I = B_z/\mu_0$ (per unit length) is induced so as to cancel the external solenoid field B_z. This current interacts with the radial component of the external field, $B_r \approx (r/2) dB_z(0,z)/dz = rB_z'/2$ to produce retarding force $F = -2\pi r I B_r = -2\pi r (B_z/\mu_0)(rB_z'/2) = \pi r^2 (B_z^2)'/2\mu_0$ per unit length. But also, $F = ma = \pi r^2 \rho \dot{v} = \pi r^2 \rho v v' = \pi r^2 \rho (v^2)'/2$, where $\rho \approx 10^4$ kg/m^3 is the mass density. This integrates to give $v^2(z) = v_{-\infty}^2 - B_z^2/\mu_0 \rho$. Thus to enter a field of $B_z = 20$T, the initial velocity would need to be at least $B_z/\sqrt{\mu_0 \rho} \approx 200$ m/s for our heavy metals.

2.5.1 Jet on Axis of a Solenoid

We model the forces on a conducting jet in a magnetic by considering only a ring (or disc) perpendicular to the axis of the jet. The ring has radius r, radial extent Δr and thickness Δz.

We first consider only motion along the axis of the ring, which we call the z axis, and which is also the axis of a solenoid magnet with field $\mathbf{B}(r, z)$.

Then the magnetic flux through the ring at position z is

$$\Phi \approx \pi r^2 B_z(0, z), \tag{18}$$

whose time rate of change is

$$\dot{\Phi} = \pi r^2 \dot{B}_z = \pi r^2 B_z' v, \tag{19}$$

where $\dot{}$ indicated differentiation with respect to time, $'$ is differentiation with respect to z, B_z stands for $B_z(0, z)$ and v is the velocity of the center of mass of the ring.

If the metal has electrical conductivity σ, then its resistance to currents around the ring is

$$R = \frac{2\pi r}{\sigma \Delta r \Delta z}, \tag{20}$$

so the (absolute value of the) induced current is

$$I = \frac{\mathcal{E}}{R} = \frac{\dot{\Phi}}{R} = \frac{\sigma r B_z' v \Delta r \Delta z}{2}. \tag{21}$$

Radial Pinch The Lorentz force on the ring due to the interaction of this current with the axial field pinches the jet radially, while that due to the interaction with the radial field opposes the motion. The radial pinch can be characterized by a radial pressure gradient,

$$\frac{\Delta P_r}{\Delta r} = \frac{\Delta F_r}{\Delta r \Delta z \Delta l} = -\frac{B_z I \Delta l}{\Delta r \Delta z \Delta l} = -\frac{\sigma r B_z B_z' v}{2}. \tag{22}$$

As the jet enters the magnet from $z = -\infty$, the axial field gradient, B_z', is initially positive, and the radial forces are inward. However, at the jet exits the solenoid, the gradient B_z' becomes negative, and the radial force is outwards. Even if the jet has not been destabilized by the pinch on entering the magnetic, the radially outward forces experienced on leaving the magnet may disperse the jet.

The pinch is greatest as the ring passes the edge of the solenoid, where $B_z \approx B_0/2$ and $B_z' \approx B_0/D$ for a solenoid of diameter D and peak axial field B_0. That is,

$$\frac{\Delta P_{r,\max}}{\Delta r} \approx -\frac{\sigma}{4}\frac{r}{D} B_0^2 v. \tag{23}$$

Integrating this over radius, the pressure gradient between the axis and radius r is

$$\Delta P_{r,\max} \approx -\frac{\sigma}{8}\frac{r^2}{D} B_0^2 v. \tag{24}$$

Axial Retarding Force The component of the Lorentz force that opposes the motion of the ring is

$$\Delta F_z = 2\pi r B_r I = -\pi\sigma r^2 B_r B_z' v \Delta r \Delta z \approx -\frac{\pi\sigma r^3 (B_z')^2 v \Delta r \Delta z}{2}, \tag{25}$$

using the approximate relation for the radial field near the z-axis,

$$B_r(r,z) \approx -\frac{r}{2}\frac{dB_z(0,z)}{dz} = -\frac{rB_z'}{2}, \tag{26}$$

(which can be deduced from the Maxwell equation $\nabla \cdot \mathbf{B} = 0$).

The equation of motion of a ring is then

$$dF_z = -\frac{\pi\sigma r^2 (B_z')^2 v_z \Delta z}{2} = m\dot{v}_z = 2\pi\rho r \Delta r \Delta z v_z' v_z, \tag{27}$$

where ρ is the mass density of the metal. After dividing out the common factor of $\pi r \Delta r \Delta z v_z$ we find

$$v_z'(r) = -\frac{\sigma r^2 (B_z')^2}{4\rho}. \tag{28}$$

Before considering detailed models of the axial field profile, B_z, we note that the peak gradient of the axial field of a solenoid of diameter D is B_0/D, and the gradient is significant over a region $\Delta z \approx D$. Hence, we estimate that on entering a solenoid the jet velocity is reduced by an increment

$$\Delta v_z(r) \approx \frac{\sigma r^2 B_0^2}{4\rho D}. \tag{29}$$

On leaving the solenoid, the jet velocity is reduced by a second increment Δv_z. (Since the effect depends on $(B_z')^2$, the sign is the same on both entering and exiting.)

The jet velocity cannot actually go negative due to the effect of the magnetic field . If the velocity reaches zero the jet stops (falls). Note that we divided eq. (27) by v_z before integrating; once v_z becomes zero F goes to zero and stays there.

The reduction of velocity is zero on axis of the jet, and grows quadratically with radius. If the jet were a rigid body, the Δv_z would be one half the value given by eq. (29) at the outer radius.

If the change in velocity is small compared to the initial velocity, $v_{-\infty}$, we estimate the distance $\Delta z(r)$ by which the material in the jet at radius r is retarded compared to the material on axis as

$$\Delta z(r) \approx \Delta v_z(r)\Delta t \approx \Delta v_z(r)\frac{D}{v_{-\infty}} \approx \frac{\sigma r^2 B_0^2}{4\rho v_{-\infty}}. \tag{30}$$

We desire this to be small compared to the length of the jet. Indeed, it will be awkward if Δ_z exceeds the radius of the jet.

We now consider more specific models.

Semi-Infinite Solenoid The fields of a semi-infinite solenoid are rather amenable to analytic calculation. Indeed, for a solenoid of radius $D/2$ with coils at $z > 0$, the axial field is

$$B_z(0,z) = \frac{B_0}{2}\left(1 + \frac{z}{\sqrt{(D/2)^2 + z^2}}\right), \tag{31}$$

whose derivative is

$$B_z' = \frac{dB_z(0,z)}{dz} = \frac{B_0}{2}\frac{(D/2)^2}{[(D/2)^2 + z^2]^{3/2}}. \tag{32}$$

Using eq. (32) in eq. (28) and integrating the equation of motion from $-\infty$ to z, we find

$$v_z(r,z) = v_{-\infty} - \frac{3\sigma r^2 B_0^2}{64\rho D}\left(\frac{\pi}{2} + \tan^{-1} w + \frac{w}{1+w^2} + \frac{2w}{3(1+w^2)^2}\right), \tag{33}$$

where D is the diameter of the solenoid and $w = 2z/D$.

The semi-infinite solenoid is meant to represent a finite solenoid of length $L = \alpha D$. Since the semi-infinite coil begins at $z = 0$, the center of the finite solenoid it approximates is at $z = \alpha D/2$, *i.e.*, at $w = \alpha$. For $\alpha \gtrsim 1$, as is reasonable for an actual magnet, there is little difference between the result of eq. (33) at $w = \alpha$ and at $+\infty$, so we estimate the change in velocity as

$$\Delta v_z(r) \approx -\frac{3\pi\sigma r^2 B_0^2}{64\rho D}. \tag{34}$$

The retardation relative to the center of the jet is related by

$$\Delta\dot{z}(r) = \Delta v_z(r) = \Delta z' v_z \approx \Delta z' v_{-\infty}, \tag{35}$$

where the approximation holds if $\Delta v_z \ll v_{-\infty}$. In this approximation, we integrate eq. (33) to find

$$\Delta z(r) \approx -\frac{3\sigma r^2 B_0^2 w}{128\rho v_{-\infty}}\left(\frac{\pi}{2} + \tan^{-1} w - \frac{1}{3w(1+w^2)}\right). \tag{36}$$

This diverges for large w, but at $w = \alpha \approx 1$, corresponding to the center of a real magnet, we have

$$\Delta z(r) \approx -\frac{3\pi\sigma r^2 B_0^2 \alpha}{128\rho v_{-\infty}}. \tag{37}$$

Numerical Examples We consider the lead-bismuth alloy 255 whose conductivity is about 10^6 MKSA units and whose density is about 10 gm/cm^3, *i.e.*, 10^4 kg/m^3. Then, eq. (34) leads to the requirement

$$v_{-\infty} > 60 \text{ m/s}\left[\frac{r}{1 \text{ cm}}\right]\left[\frac{r}{D}\right]\left[\frac{B_0}{20 \text{ T}}\right]^2. \tag{38}$$

It is thought that the jet radius must be 0.5-1 cm to match the proton beam, and that the inside diameter of the solenoid will be about 20 cm. In this case we need $v_{-\infty} > 0.75$-3 m/s for $B_0 = 20$ T.

Again, if the jet is to exit the magnet, $v_{-\infty}$ must be twice the minimum given in (38).

In the approximation of eq. (37), the shear in the jet profile between its axis and radius r is

$$\frac{\Delta z(r)}{r} \approx -3\alpha\left[\frac{r}{1 \text{ cm}}\right]\left[\frac{B_0}{20 \text{ T}}\right]^2\left[\frac{10 \text{ m/s}}{v_{-\infty}}\right]. \tag{39}$$

For, say, $r = 1$ cm, $v_{-\infty} = 10$ m/s, $\alpha = 2$ and $B_0 = 20$ T, we would have $\Delta z(r) \approx 6r$, which is a fairly severe distortion of the jet.

Returning to the issue of the radial pinch, we can now cast eq. (24) in the form

$$\Delta P_{r,\max} \approx 50 \text{ atm.} \left[\frac{r}{1 \text{ cm}}\right] \left[\frac{r}{D}\right] \left[\frac{B_0}{20 \text{ T}}\right]^2 \left[\frac{v_{-\infty}}{10 \text{ m/s}}\right]. \tag{40}$$

For, say, $r = 1$ cm, $v_{-\infty} = 10$ m/s, $D = 20$ cm and $B_0 = 20$ T, the maximum radial pressure is 2.5 atmosphere. While not large, this may still be enough to perturb the shape of the jet as it enters the magnet.

When the jet leaves the magnet, the radial pressure goes negative. This pressure is still small compares to the tensile strength of the jet material, so the jet will not necessarily tear apart. However, the rapid change of pressure from positive to negative may excite oscillations of the jet which lead to breakup into macroscopic droplets. This would occur after the proton beam interacted with the jet, so is more of a nuisance for the liquid collection system than a fundamental flaw.

The longitudinal effects, (38) and (39), are suppressed at higher jet velocities, which, however, enhances the radial pinch (40).

2.5.2 Jet at an Angle to the Axis of a Solenoid

To improve the yield of pions in the interaction of the proton beam with the liquid jet, it is desirable that the jet axis make a small angle $\theta \approx 0.1$ to the axis of the solenoid. In this case the motion of the jet includes a component at right angles to the magnetic field.

The induced eddy currents will flow in loops that are roughly perpendicular to the magnetic field lines. As a simplification, we suppose that the current loops are circles perpendicular to the axis of the solenoid. This approximation should be reasonable for small θ.

The (unperturbed) trajectory of the conductor of radius a is taken to be along the line

$$x = z\theta, \tag{41}$$

where z increases with increasing time. To simplify the calculations, we suppose the trajectory follows eq. (41) even though the velocity of the jet is perturbed by the magnetic field (impulse approximation).

Following the same line of argument as in sec. 2.5.1 we again calculate the drag force induced on the conducting disc. The force element on a piece of the disk at radius $r = \epsilon a$ and azimuth ϕ is found to be [19]

$$\begin{aligned} d\mathbf{F} &= I d\mathbf{l} \times \mathbf{B} \qquad\qquad (42)\\ &= I\epsilon a d\phi \left[(\hat{\mathbf{x}} \cos\phi + \hat{\mathbf{y}} \sin\phi) \left(B_z - \frac{(z\theta)^2 + (\epsilon a)^2 + 2\epsilon a z\theta\cos\phi}{4} B_z'' \right) + \hat{\mathbf{z}} \frac{B_z'}{2} (\epsilon a + z\theta \cos\phi) \right], \end{aligned}$$

where $\hat{\rho}$ is the unit vector pointing radially outwards from the axis of the jet ($\rho = \epsilon a$).

The transverse force can be decomposed into a radial pinch (or expansion) as discussed in sec. 2.5.1 plus a drag in the x direction. The longitudinal (z) force vanishes on the axis of the jet, has a drag that is independent of azimuth, and another component that varies with azimuth causing a torque (or shear).

Drag Forces We first ignore the radial pinch and the shear by integrating eq. (43) over ϕ and using eq. (21) for I to obtain

$$d\mathbf{F} = \frac{\pi\sigma a^4 v_z B_z' \epsilon^3 \Delta\epsilon \Delta z}{2} \left(\hat{\mathbf{x}} \frac{z\theta B_z''}{2} - \hat{\mathbf{z}} B_z' \right). \tag{43}$$

The z component of the drag force is the same as found previously in eq. (25). The retarding force vanishes on the jet axis, and increases as the cube of the radius within the jet. As a result, the core of the jet will move ahead of the outer regions.

In turn, we integrate this over ϵ to obtain the total force on a disc of thickness Δz:

$$\mathbf{F} = \frac{\pi\sigma a^4 v_z B_z' \Delta z}{8} \left(\hat{\mathbf{x}} \frac{z\theta B_z''}{2} - \hat{\mathbf{z}} B_z' \right). \tag{44}$$

In the equation of motion, we again replace differentiation by time with that by z:

$$\mathbf{F} = m\dot{\mathbf{v}} = \pi a^2 \Delta z \rho v_z \mathbf{v}'. \tag{45}$$

The components of the equation of motion of the conducting jet are thus,

$$v_x' = \frac{\sigma a^2 z\theta B_z' B_z''}{16\rho}, \qquad \text{and} \qquad v_z' = -\frac{\sigma a^2 (B_z')^2}{8\rho}. \tag{46}$$

We will use the example of a semi-infinite solenoid to illustrate the effect of the eddy currents on the jet velocity, because the needed field derivatives have simple analytic forms. The form of the trajectory, (41), assumes that the center of the magnet is at the origin. Suppose the length of the physical magnet is α times its diameter D, so that the coil extends over $-\alpha D/2 \leq z \leq \alpha D/2$. Then the field of the physical magnet can be represented by the field of a semi-infinite solenoid whose coil begins at $z = -\alpha D/2$.

From the derivatives of eq. (31) we see that v_z' is always negative but that v_x' is negative only until the jet enters the magnet ($z = -\alpha D/2$). Integrating (46) from $-\infty$ to z, we find that the velocity components of the jet are

$$v_x = v_{x,-\infty} - \frac{3\sigma a^2 B_0^2 \theta}{1024\rho D} \left[\frac{\pi}{2} + \tan^{-1} w + \frac{w}{1+w^2} + \frac{2w}{3(1+w^2)^2} - \frac{16z}{3D(1+w^2)^3} \right], \tag{47}$$

and

$$v_z = v_{z,-\infty} - \frac{3\sigma a^2 B_0^2}{128\rho D} \left[\frac{\pi}{2} + \tan^{-1} w + \frac{w}{1+w^2} + \frac{2w}{3(1+w^2)^2} \right], \tag{48}$$

where $w = 2z/D + \alpha$. Of course, $v_{x,-\infty} = \theta v_{z,-\infty}$ by assumption. The velocity components of the jet when it reaches the center of the magnet ($z = 0,\ w = \alpha$) are

$$v_{x,0} = \theta v_{z,-\infty} - \frac{3\sigma a^2 B_0^2 \theta}{1024\rho D} \left[\frac{\pi}{2} + \tan^{-1} \alpha + \frac{\alpha}{1+\alpha^2} + \frac{2\alpha}{3(1+\alpha^2)^2} \right], \tag{49}$$

and

$$v_{z,0} = v_{z,-\infty} - \frac{3\sigma a^2 B_0^2}{128\rho D} \left[\frac{\pi}{2} + \tan^{-1} \alpha + \frac{\alpha}{1+\alpha^2} + \frac{2\alpha}{3(1+\alpha^2)^2} \right], \tag{50}$$

Thus, while both v_x and v_z are reduced on entering the solenoid, the relative reduction in the x velocity is only 1/8 that of the z velocity. As a consequence, the angle θ of the trajectory to the axis of the solenoid actually increases as the jet enters the magnet. For example, suppose that $v_{z,-\infty}$ is 3 times the loss of velocity on entering the magnet. Then

$$v_{z,0} = \frac{2}{3} v_{z,-\infty}, \qquad v_{x,0} = \frac{23}{24} \theta v_{z,-\infty}, \tag{51}$$

and the angle of the trajectory at the center of the magnet is

$$\theta_0 = \frac{v_{x,0}}{v_{z,0}} = \frac{69}{48}\theta = 1.44\theta. \tag{52}$$

Figure 16 illustrates the variation of v_x, v_z and θ of the jet as a function of z.

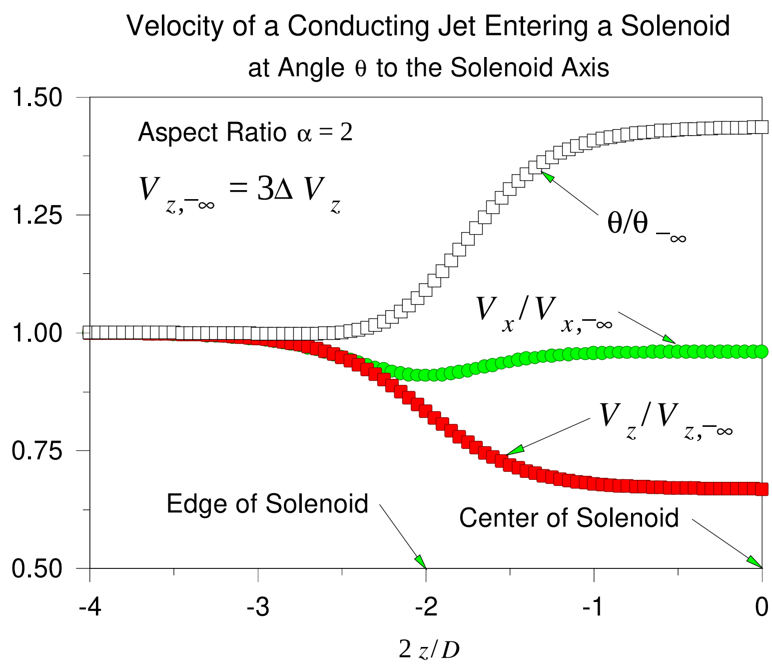

Figure 16: v_x, v_z and θ of the jet as a function of z as it enters a solenoid of aspect ratio $\alpha = 2$, according to eqs. (47-48). The initial z velocity of the jet is taken to be 3 times the loss of velocity on entering the solenoid.

We are greatly encouraged by these idealized calculations that the effect of eddy currents on the transverse velocity of the jet will not be too severe.

The above analysis is only for the drag force on the jet as a whole. Recall that the force varies with radius within the jet, and so leads to longitudinal distortions as discussed in sec. 2.5.1. The variation of the drag force in x leads to additional torques and shears, which we now discuss.

Torque and Shear The magnetic forces on the eddy currents also produce a torque that will twist the jet about the axis perpendicular to the plane of the jet motion – the y axis in our example.

The torque $d\mathbf{N}$ on a small element of a current ring about its center can be calculated from eq. (43). On integrating over ϕ and ϵ we find that $N_x = 0$ and the total torque on a disc of radius a and thickness Δz is

$$N_y = \frac{\pi}{16} z\theta\sigma a^4 v_z B_z'^2 \Delta z \approx \frac{xF_z}{2}. \tag{53}$$

The sense of rotation is to align the axis of the jet with the axis of the magnet as the jet enters the field.

The moment of inertia of the disc about a diameter is $ma^2/4 = \pi\rho a^4 \Delta z/4$. Hence the angular acceleration of the azimuthal angle φ of the disc about the y axis is

$$\ddot{\varphi} = v_z \frac{d\dot{\varphi}}{dz} = \frac{\theta\sigma z B_z'^2 v_z}{4\rho}, \tag{54}$$

which is independent of the radius of the jet. Using B_z' from eq. (31), we have

$$\frac{d\dot{\varphi}}{dz} = \frac{\theta\sigma B_0^2}{4\rho D^2} \frac{z}{(1+w^2)^3}, \tag{55}$$

where as before, $w = 2z/D + \alpha$ and $\alpha = L/D$. This can be integrated once to give

$$\dot{\varphi} = v_z \frac{d\varphi}{dz} = -\frac{3\theta\sigma B_0^2}{128\rho} \left[\frac{\alpha\pi}{2} + \alpha \tan^{-1} w + \frac{\alpha w}{1+w^2} + \frac{2(1+\alpha w)}{3(1+w^2)^2} \right]. \tag{56}$$

If we ignore the variation in v_z with position, this can be integrated once more to yield

$$\varphi(z) = -\frac{3\theta\sigma B_0^2 D}{256\rho v_z} \left[\left(\alpha w + \frac{1}{3}\right) \left(\frac{\pi}{2} + \tan^{-1} w\right) + \frac{\alpha - w}{3(1+w^2)} \right]. \tag{57}$$

At the center of the magnet, $w = \alpha$, the total angle of rotation of the disc is

$$\varphi_{\text{center}} = -\frac{3\theta\sigma B_0^2 D}{256\rho v_z} \left[\left(\alpha^2 + \frac{1}{3}\right) \left(\frac{\pi}{2} + \tan^{-1} \alpha\right) \right] \approx -\frac{3\pi\alpha^2\theta\sigma B_0^2 D}{256\rho v_z}, \tag{58}$$

where the approximation holds for α somewhat larger than 1. For example, if $\alpha = L/D = 2$, $D = 0.2$ m, $B_0 = 20$ T and $v_z = 10$ m/s, we find $\varphi_{\text{center}} \approx -4\pi\theta$. With $\theta = 0.1$ rad, then $\varphi_{\text{center}} \approx -0.4\pi$.

Equation (56) indicates the interesting result that the rate of change of rotation is independent of the velocity, so the total rotation can be suppressed by increasing the jet velocity, lowering the transit time.

A liquid jet would presumably not rotate. Rather, there would be a shear, in which the portion of the jet closer to the axis is retarded more than that farther out. Our estimate that $\varphi_{\text{center}} \approx 90°$ can perhaps be reinterpreted as indicating that the shear distance along the jet axis will amount to roughly the jet radius when the jet reaches the center of the magnet. This would not be troublesome.

2.5.3 The Rayleigh Instability of the Jet

Zero Magnetic Field Following earlier work by Plateau, Rayleigh deduced that a cylindrical jet is unstable against perturbations of wavelength (along the jet axis) greater than the circumference of the jet [81]. The result of the instability is the breakup of the jet into droplets, commonly seen as water exits a nozzle. The characteristic time for onset of the instability is

$$\tau = 3\sqrt{\frac{r^3\rho}{T}}, \tag{59}$$

where the jet has radius r, mass density ρ and surface tension T. The length of the jet before breakup is then $v\tau$, where v is the velocity.

An example of breakup of a 0.5-mm-diameter mercury jet has been reported by Rose *et al.* [82, 83, 84], as shown in Fig. 17. The density of mercury is $\rho = 13.5$ g/cm^3 and the surface tension is $T = 470$ dyne/cm. Then eq. (59) gives $\tau = 0.002$ s for $r = 0.025$ cm. At 40 psi, the jet velocity was $v = 5$ m/s, so the characteristic length before breakup is predicted to be 1 cm, in good agreement with the value 1.4 cm reported by Ansley *et al.* It thus appears that Rayleigh's formula is valid for liquid metal jets.

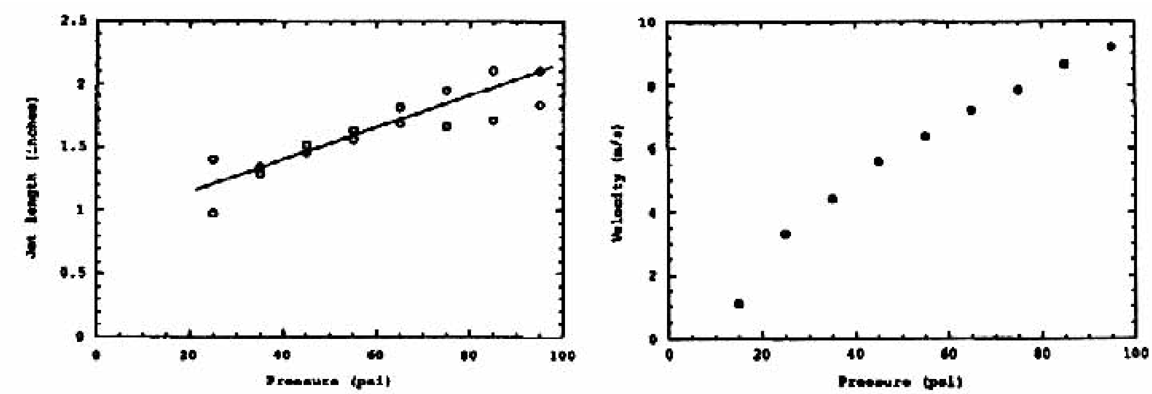

Figure 17: Length before breakup, and velocity of a mercury jet of radius 0.025 cm.

Turning to parameters relevant to the muon collider target, consider a gallium jet of radius 1 cm. The density is $\rho = 6$ g/cm^2, and the surface tension is $T = 360$ dyne/cm. Then the instability time is $\tau = 0.4$ s. For a jet velocity of 10 m/s, the breakup length would be about 4 m, which is satisfactory. If the jet radius is reduced to 0.5 cm, the breakup length drops to 1.4 m.

Nonzero Axial Magnetic Field The effect of a uniform axial magnetic field on the Rayleigh instability has been considered by Chandrasekhar [85]. There is no change in the instability time for a nonconducting liquid unless its permeability is significantly greater the 1. For a conducting liquid, Chandrasekhar introduces a quality factor,

$$Q = \frac{\mu B^2}{4\pi\eta}\sqrt{\frac{r^3}{\rho T}}, \tag{60}$$

where μ is the permeability, B is the axial magnetic field strength, and η is called the "resistivity" ($\eta = c^2/4\pi\sigma$, where σ is the electrical conductivity). For $Q > 20$, the Rayleigh instability is suppressed in the first approximation.

For mercury, $\eta = 7.5 \times 10^3$ cm^2/s and $Q = 1.33 \times 10^{-7} B^2 r^{3/2}$ in Gaussian units. Thus for a 20-T axial magnetic field and $r = 1$ cm, $Q \approx 5000$, and the Rayleigh instability should be almost completely damped. This conclusion is little changed by variations in the radius or resistivity by factors of 2, and should be valid for all liquid metal jets under consideration here.

The quality factor reaches 20 in fields slightly over 1 T (for $r = 1$ cm). Hence, unless the jet nozzle is more than a meter away from the region where the magnetic field exceeds 1 T, the Rayleigh instability will be of little concern for us.

It remains that the jet may be significantly perturbed by the nonuniform magnetic field as discussed in sec. 2.5, and/or by the thermal shock mentioned in sec. 2.1.2.

2.6 The Operation of an RF Cavity near a Target

Once the pions have been collected at the target, it is necessary to shape the collected pion/muon beam into a longitudinal phase space suitable for eventual acceleration in the following cooling section. The goal is to capture and maintain the longitudinal phase space such that the energy spread dE/E is reduced to near 10% and the pulse is contained within a pulse length of $c\tau < 6$ m. Since we are interested in capturing low-energy pions (kinetic energy 50-400 MeV), these pions will have a large initial velocity spread (β between 0.7 and 0.98). It is therefore important to begin compressing the energy spread in the phase-rotation section as soon a practical with an accelerating gradient as high as possible.

The wavelengths of the rf cavities are constrained by the requirement that $\lambda_{\rm rf}/2$ be greater than the bunch length of the collected pions/muons. This bunch length in turn is determined by the initial bunch length of the proton beam impinging on the target and the drift distance to the initial rf cavity. For an initial proton bunch length τ_{rms} of 1 ns and a drift distance of 3 m this total bunch length will be 4 ns (1.2 m). This constrains the wavelength of the initial rf cavity to be greater than ≈ 2.4 m (frequency < 125 MHz. As the beam moves down the phase-rotation channel, it will continue to spread in length and therefore the rf wavelength of subsequent rf cells will need to increase, and a complete phase-rotation scenario will require many rf cells of different frequencies.

A further constraint is placed on the frequencies of the rf cells if we add the requirement that the same phase-rotation channel must be capable of handling both positive and negative bunches in separate beam spills. This constraint can be simply satisfied by requiring the set of cavities to be odd multiples of a fundamental harmonic, *e.g.*, 20, 60, 100, 140 MHz, *etc.*, or 10, 30, 50, 70, 90, 110 MHz, *etc.*We chose for convenience the series based on the fundamental harmonic of 10 MHz. In such a scenario, the beginning rf frequency could be 110 MHz, descending to a final rf frequency of 10 MHz. Parameters for a possible complete scenario is given in the Table 2.6.

For the $\mu^+\mu^-$ collection system to be viable, we must satisfy ourselves that the rf cells will work at the levels required of them and in particular that the initial rf cells will perform as expected in the high-radiation environment immediately following the target. Since experience operating an rf cell in a high-radiation environment generated by a 10^{14} *ppp*

Table 5: Low-Energy Collection-Linac Parameters

rf Frequency (MHz)	90	50	30
Cavity Length (cm)	120	120	120
Full Gap length (cm)	36	36	36
Cavity Radius (cm)	90	206	126
Beam Pipe Aperture (cm)	30	30	30
$Q/1000$ (from SFISH)	53.4	71.1	16.8
Ave Gradient (MV/m)	4.2	4.0	2.1
RF Peak Power (MW)	1.8	1.2	4.8
Ave Power @ 15 Hz (kW)	2.4	7.8	12.6
Stored Energy (J)	166	260	418
Linac Segment (m)	6	18	18
Total Power @ 15Hz (kW)	12	118	190

beam is limited, we propose to establish a proof-of-principle demonstration of this issue by constructing and operating at high gradients an rf cavity with a frequency suitable for a muon-collider collection system.

3 The R&D Program

The proposed R&D program into targetry issues for a muon collider consists of eight parts:

1. Initial studies of liquid (and solid) target materials with a proton beam at the AGS.
2. Studies of a liquid-metal jet entering a 20-T magnet (at the FSU magnet lab).
3. Studies of a liquid-metal jet + proton beam, but without magnetic field.
4. Studies of liquid-metal jet + proton beam + 20-T pulsed solenoid magnet.
5. Studies of a 70-MHz rf cavity (or cavities) downstream of target in proton beam – but without a magnet around the cavity. .
6. Add a 1.25-T, 1.25-m-radius magnet to item 5.
7. Characterization of the pion yield downstream of target + rf cavity.
8. Simulation of performance of liquid-metal targets: thermal shock, eddy currents.

3.1 Initial Studies of Targets in a Proton Beam

The first set of studies concerns the viability of various target options as concerns their interaction with the proton beam. The key issues are the effects of "thermal shock" (sec. 2.1.2), and (for solid targets) the effects of radiation damage. We propose to study four target geometries:

1. **A free liquid-metal jet.** The jet may be dispersed by the beam, possibly violently. The 20-T magnetic field should damp the dispersal, but also distorts the jet on entry into the field. jet. possible).

2. **Liquid-Metal in a pipe.** There is a high probability of damage to the pipe by the beam-induced thermal-shock.

3. **A cylindrical solid target.** The cylindrical geometry may enhance beam-induce thermal-shock damage along the axis of the target.

4. **A rectangular solid target.** For the energy deposition required at a muon collider source, thermal-shock damage is not expected. If confirmed, the primary concern will then be the long-term effect of radiation damage on the mechanical integrity of a moving band target.

Details of the test targets will be presented after a discussion of the beam.

3.1.1 The Proton Testbeam

The test beam should approach as closely as possible the parameters of the primary proton beam for a muon collider. The key parameters are 16-24 GeV energy, 10^{14} protons per pulse, rms radius of 4 mm and pulse length of 2 ns.

The candidate proton testbeam is the FEB U-line at the AGS, shown in Fig. 18. The location of the U-line in the AGS-RHIC complex can be seen in Fig. 26. This beam is typically operated at 24 GeV, extracting a single pulse from the AGS with up to 1.6×10^{13} protons in that pulse. The beam emittance is about 100π mm-mrad and the pulse length is typically about 25 ns(?). The pulse rate can be as high as 0.7 Hz (2 Hz??).

All of the beam tests presented in this proposal can be performed during parasitic use of the beam at a pulse rate of one every two minutes, or less. The initial studies (secs. 3.1 and 3.3) are in effect a series of single-pulse experiments, while later studies (secs. 3.4-7) will be limited by the repetition rate of the pulsed 20-T magnet.

The individual pulse length, if tens of ns or less, is not of concern until studes of the behavior of an rf cavity (secs. 3.5-6). A recent study [86] indicates that the bunch length in the AGS be reduced to $\sigma_t = 2$ ns, which will be adequate even for the rf-cavity studies.

The AGS beam energy of 24 GeV is well matched to the needs of a muon-collider source [1, 90]; see also Appendix B.

The remaining beam issue is whether a proton bunch in the FEB U-line can cause thermal shock at the level to be encountered at a muon-collider source. According to the model presented in sec. 2.1.2, the pressure in the target material resulting from the thermal shock is proportional to the peak density of energy desposited (Joules/g), rather than, say, the total energy deposited. Hence, by focusing the

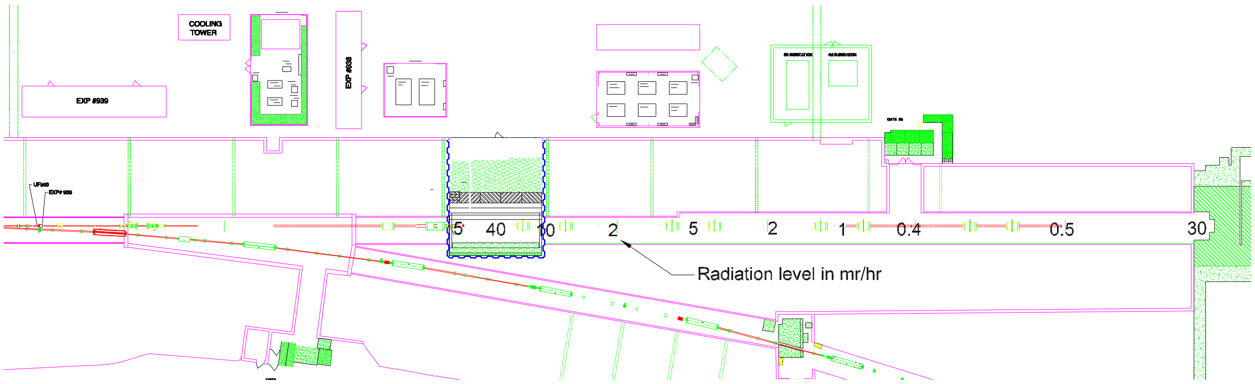

Figure 18: Plan view of FEB U-line at the BNL AGS. Residual radiation level at various point along the tunnel are indicated.

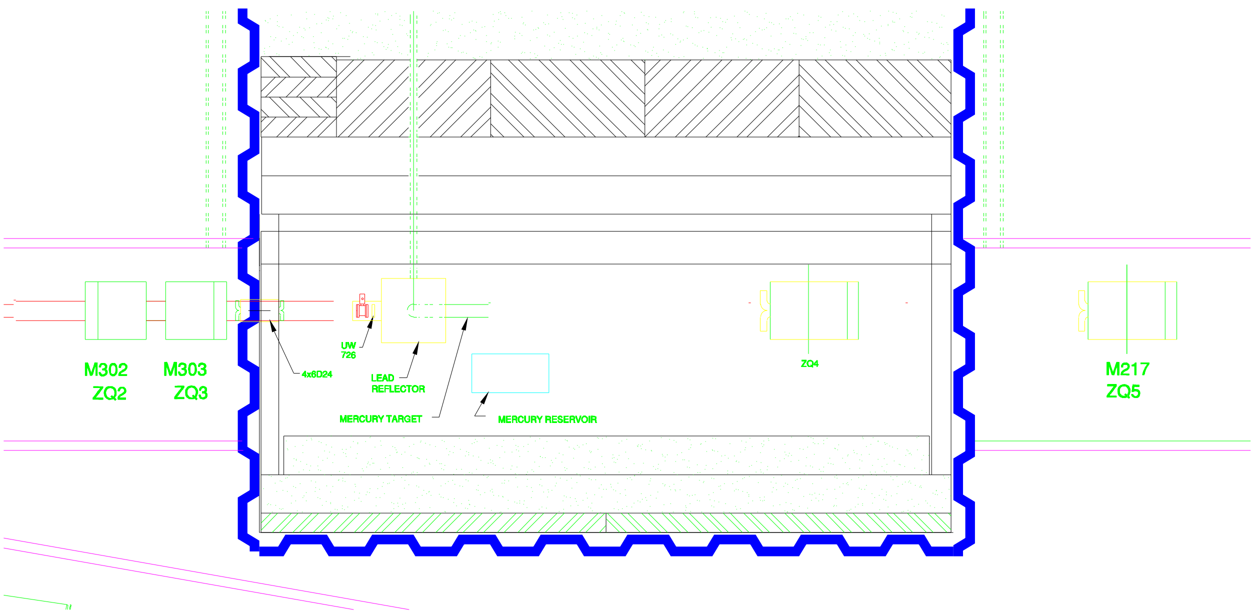

Figure 19: The neutrino blockhouse of the FEB U-line, where tests of a mercury target for neutron spallation have been performed recently.

3.2 Liquid-Metal Jet with a 20-T Magnet

3.3 Liquid-Metal Jet with a Proton Beam

3.4 Liquid-Metal Jet with a Proton Beam in a 20-T Magnet

3.5 RF Cavity near the Target

For the $\mu^+\mu^-$ collection system discussed in sec. 2.6 to be viable, we must satisfy ourselves that the rf cells will work at the levels required of them and in particular that the initial rf cells will perform as expected in the high-radiation environment immediately following the

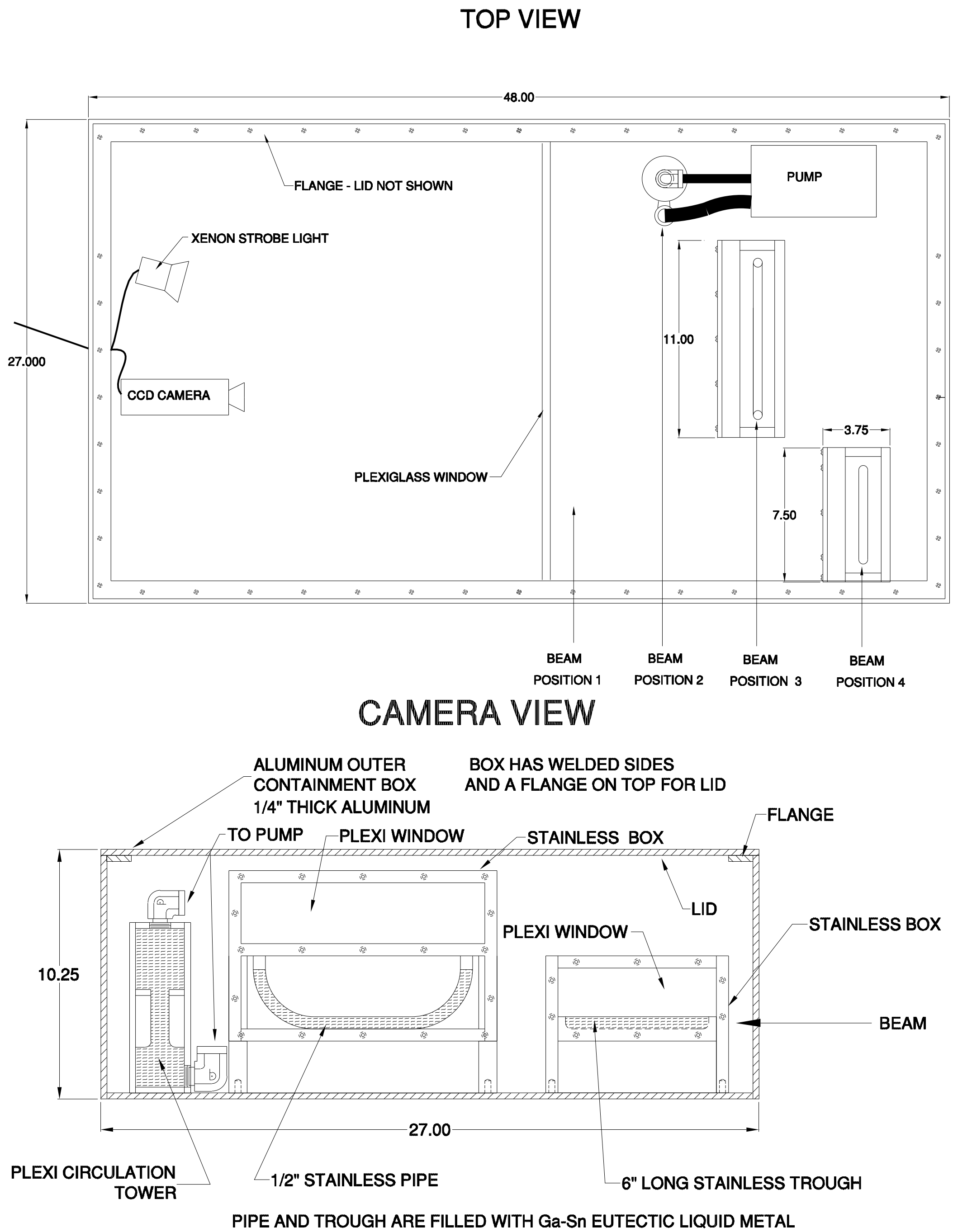

Figure 20: Top and beam views of the setup to test simple liquid targets.

target. Since experience operating an rf cell in a high-radiation environment generated by a 10^{14} ppp beam is limited, we propose to establish a proof-of-principle demonstration of this issue by constructing and operating at high gradients an rf cavity with a frequency suitable for a muon-collider collection system.

A key issue is the rf power required for such a test. A search of available rf sources in the

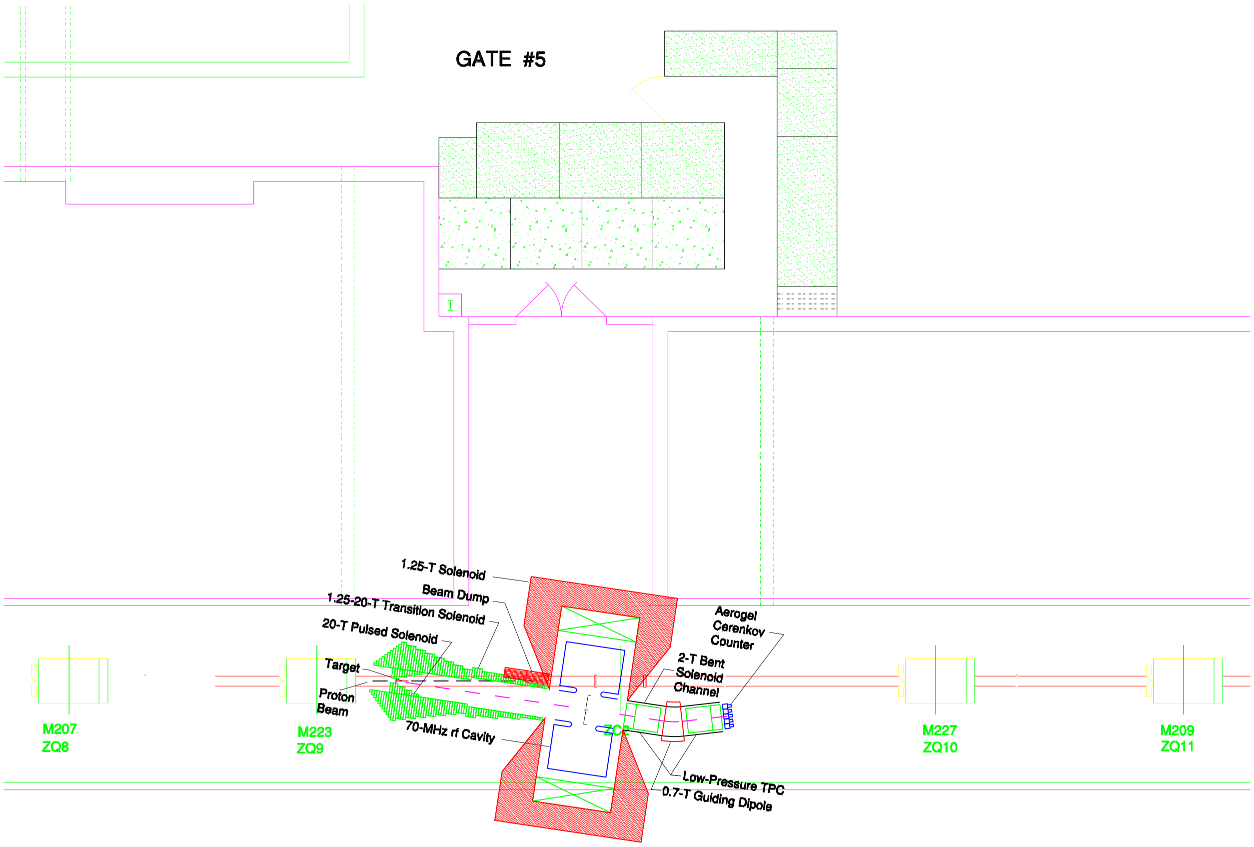

Figure 21: Possible arrangement of the targetry experiment near Gate #5 in the FEB U-line.

upper frequency range of our requirements has led us to a 70-MHz rf power source which is now available at LBL as the result of retirement of the HILAC facility. We therefore focus our efforts on the design and utilization of system using this frequency. As a base line we consider an rf accelerating cell with parameters given in Table 3.5. This cavity is shown in Fig. 22.

The above parameters are valid for operating the rf cavity at a level of 2 Kilpatricks (corresponding to peak wall electric gradients of 20 MV/m). For testing purposes, it would be of interest to run the cavity at the highest possible peak-power levels in order to obtain the maximum accelerating gradient at the front end. The R&D program would entail constructing a 70-MHz rf cavity, powering it to maximum power levels without beam/target interactions and then determine the maximum power levels achievable with the high-radiation environment present with beam/target interactions.

A further requirement of the phase-rotation channel is to envelope the entire rf channel within a solenoidal field of 1.25 T. It is desirable to have this field be as uniform as possible in order to avoid particle losses through resonant effects. These effects are pronounced if, for example, one places solenoid coils between the rf cells thereby giving the longitudinal structure of the solenoidal field an oscillating structure with amplitude variations (see Fig. 24). We avoid this problem by placing the entire rf channel within the coils of the solenoids with

Table 6: 70-MHz rf-Cavity Parameters

RF frequency (MHz)	70
Cavity Length (cm)	120
Full Gap length (cm)	50
Cavity Radius (cm)	125
Beam Pipe Full Aperture (cm)	60
$Q/1000$ (from SFISH)	63.1
Ave Gradient (MV/m)	5.0
RF Peak Power (MW)	2.4
Stored Energy (J)	330

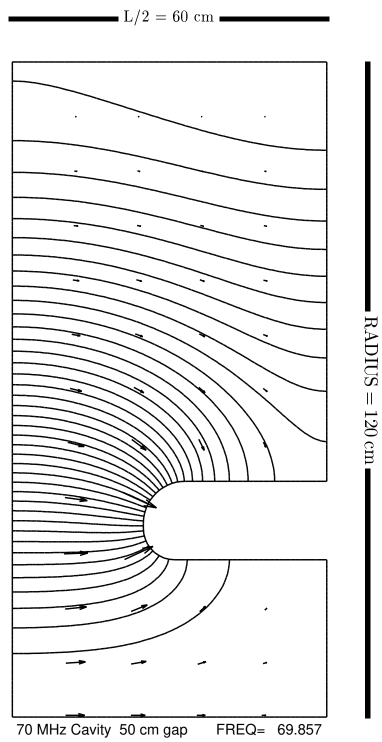

Figure 22: Superfish solution for a 70-MHz rf cavity.

the penalty of increasing the warm bore aperture of the solenoids.

We consider two variations of solenoids with the 240-cm warmbore aperture required to fully envelope the 70-MHz rf cell. A superconducting solenoid with such an aperture capable of generating a 1.25 T field can be constructed at a cost of \$1.2 M. A conventional solenoid would be very similar to that now used in BNL experiment E-787, and is sketched in Fig. 25.

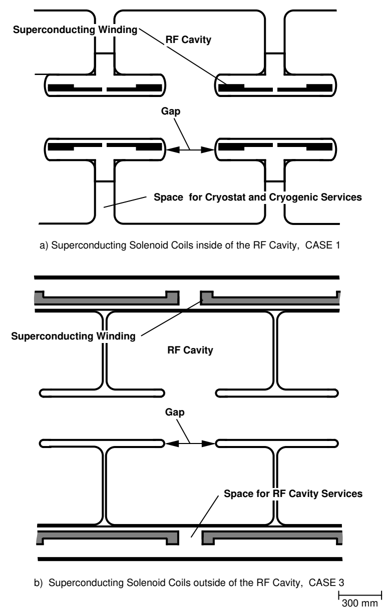

Figure 23: Different locations of solenoid coils for a phase-rotation system.

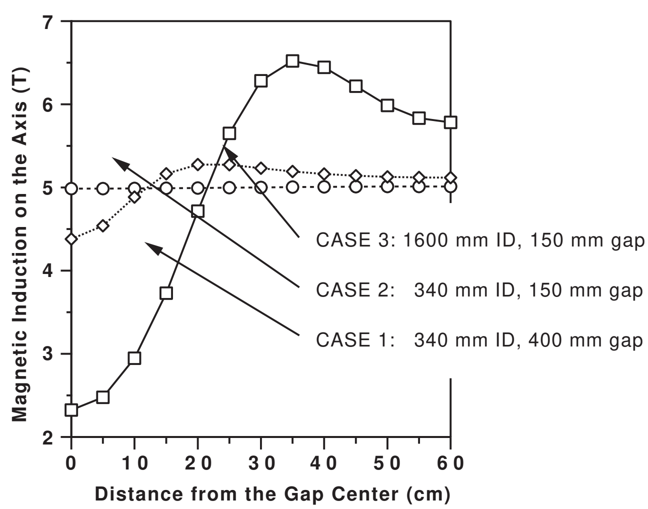

Figure 24: Magnetic induction along the beam axis for three different coil-placement scenarios.

3.6 RF Cavity Inside a 1.25-T Magnet near the Target

3.7 Characterization of the Pion Yield from the Target

We propose as a final phase in the R&D program to measure the pion yield produced and collected by the prototype system. The number of captured pion/muons per incident proton is a critical parameter for the success of a muon collider. A measurement of this quantity would provide a useful check on previous measurements of the pion production yield and on the simulation codes used for designing the collection system. Another goal of the experiment is to calibrate high-current diagnostic devices that will be required for monitoring operation of the target and capture system in normal operation.

3.7.1 Overview

The quantity we wish to measure is $dN_\pi(B)/dPrdrd\phi$, where $N_\pi(B)$ is the number of identified pions (or muons) for a peak field B in the collection solenoid, dP is the momentum bin, and $rdrd\phi$ is the bin in cross sectional area at some plane following the collection system. The asymmetry of the production target with respect to the axis of the solenoid causes the distribution to be non-uniform in azimuthal angle ϕ.

As a primary requirement, we seek a momentum resolution of $\sigma_P/P \leq 0.05$ over the entire momentum interval $100 < P_\pi < 500$ MeV/c. Another important constraint on the detector design is the need to distinguish pions and muons from other particles (electrons, protons, Kaons), although we need not distinguish between pions and muons

A schematic drawing of the proposed experiment is shown in Fig. 25.

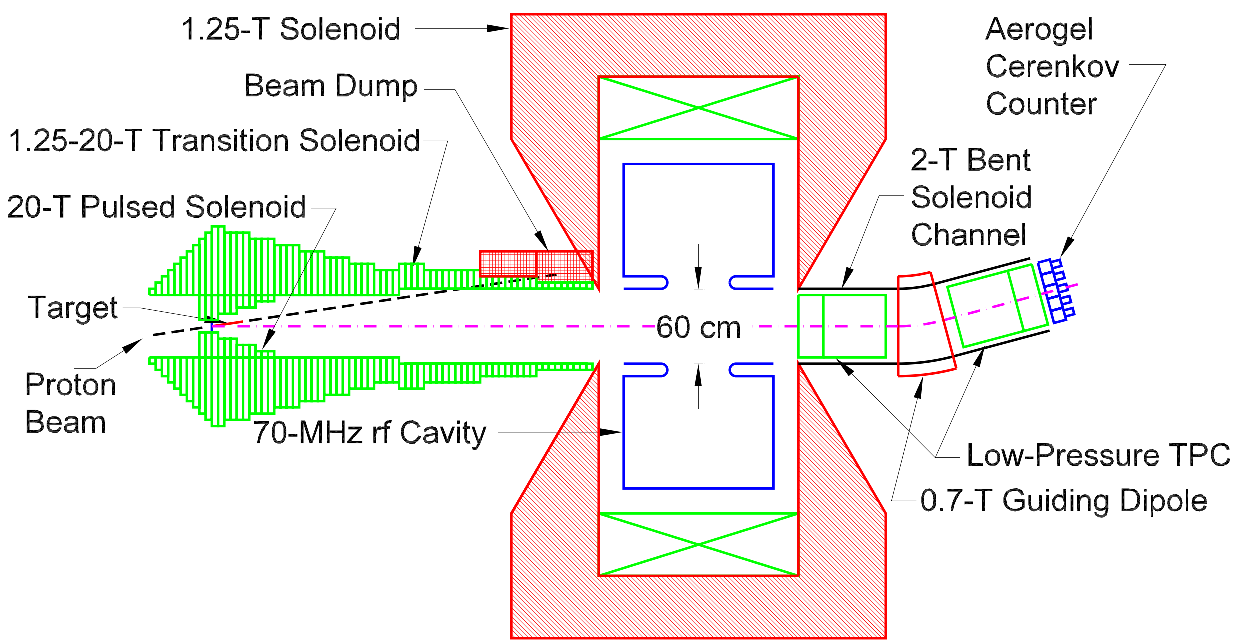

Figure 25: Plan view of the full configuration of the targetry experiment. *Details of this figure now match one of the scenarios discussed in the text.*

3.7.2 AGS Beam Requirements

Unlike the previous parts of the proposal, the characterization of the pion yield will require slow extracted beam. This has not been available up to now in the U-line, but discussions with AGS staff indicate that some ideas have been considered for this (*need clarification* *here*). We would need only a few times 10^5 protons per pulse (so as to have only about one interaction during the 8-μs drift time of the TPC's in the detector). For compatibility with the pulsed solenoid the protons should be uniformly distributed over a $\approx$ 400-ms spill. The repetition rate required is only 10/hour. The spot size on the target should be ≈ 0.5 cm^2 ($\sigma_r \approx 4$ mm).

3.7.3 Momentum Spectrometer

Since the target and rf cavity are already enclosed in a solenoidal field, it is natural to use a bent solenoid to provide the dispersion needed in the spectrometer. Particle-position measurements will be made using two Time Projection Chambers (TPC's) that surround a bend in the solenoid channel. This spectrometer arrangement is similar to one proposed for the Ionization Cooling Test Facility (MUCOOL) experiment [6, 93] at FNAL.

General Features of a Bent Solenoid. In any solenoid individual charged particles undergo helical trajectories around some "guide" trajectory. In a bent solenoid the guide trajectory is deflected perpendicular to the plane of the bend of the solenoid, taken to be the horizontal (x-z) plane. This deflection is known as "curvature drift" and the amount of deflection is proportional to the particle's momentum.

If a vertical dipole field is superimposed over the curved part of the solenoid, one reference momentum P_0 will pass through with its guide trajectory undeflected [93]. Particles with momenta $P < P_0$ will have their guide trajectory deflected in one direction vertically, while those with $P > P_0$ will have their guide trajectory deflected in the other direction. We take the reference momentum for the spectrometer to be $P_0 = 300$ MeV/c, since that is the center of the momentum range of interest. The guide dipole field that leaves the reference momentum undeflected in a solenoid whose bend has radius of curvature $R_{\rm bend}$ is [93]

$$B_G = \frac{P_0}{eR_{\rm bend}}. \tag{61}$$

For example, with $P_0 = 300$ MeV/c and $R_{\rm bend} = 1.4$ m, we find that $B_G = 0.714$ T.

The vertical deflection of the guide trajectory of an off-momentum particle is given by

$$y_G = \frac{P_0}{eB_S}\frac{\Delta P}{P_0}\theta_{\rm bend}, \tag{62}$$

where B_S is the solenoid field strength and $\theta_{\rm bend}$ is the bend angle (in the plane of the bent solenoid). It is noteworthy that the deflection is greater for weaker fields. However, the momentum resolution obtainable in a spectrometer based on a bent solenoid varies as $1/(B_S\theta_{\rm bend}$, so that a stronger field gives better resolution (eq. (66) below) as is to be expected [93].

While the beam is contained within a circular aperture, defined as R_S prior to the bend, the effect of the deflection is to deform the beam into an ellipse with semimajor axis $R_S + y_G$ after the bend. The downstream solenoid and detector must be large enough to accommodate this. Hence, we desire to minimize both R_S and y_G, which implies large B_S, but small $\theta_{\rm bend}$.

Individual particles undergo Larmor oscillations around the guide trajectories with radius of curvature given by

$$R_{\rm Larm} = \frac{P_\perp}{eB_S}. \tag{63}$$

Since the product $B_S R^2_{\rm Larm} \propto P_\perp R_{\rm Larm}$ is adiabatically invariant, and we must have $R_S \geq R_{\rm Larm}$, we obtain the relation

$$B_S R_S^2 = \text{constant}. \tag{64}$$

The weight of the coil of the bent solenoid varies roughly as R_S, while the power consumed (by a resistive coil) varies as roughly as $B_S^2 R_S$. Then according to eq. (38), the power consumption will vary roughly as $B_S^{3/2}$. In general, this favors a lower-field, more massive coil. *Present a more detailed analysis....*

In the present case, particle trajectories evolve adiabatically from the capture solenoid whose field is $B_{S,0} = 20T$ to the spectrometer solenoid, so eq. (38) also tells us that

$$R_S(B_S) = R_{S,0}\sqrt{\frac{B_{S,0}}{B_S}}. \tag{65}$$

The aperture of the capture solenoid is $R_{S,0} = 7.5$ cm, corresponding to good capture efficiency up to transverse momentum $P_{\perp,0} = 225$ MeV/c.

Thus, if we choose $B_S = 2$ T for the spectrometer solenoid we will have $R_S = 24$ cm, compared to $R_S = 30$ cm in the 1.25-T magnet surrounding the rf cavity.

From the adiabatic invariance we also expect the maximum transverse momentum of particles transmitted to a 2-T spectrometer to be 70 MeV/c and the maximum Larmor radius to be 11.7 cm.

The bend angle should be large to improve the momentum resolution, but small to minimize the vertical dispersion of the beam. We choose $\theta_{\rm bend}$ as a reasonable compromise. Then for the maximum momentum deviation of 67% from the reference momentum, the guide trajectory is deflected vertically by 9 cm. Thus, after the bend the radius R_S of a circular aperture would need to be 24 + 9 = 33 cm for full acceptance. However, since the dispersion only occurs in the vertical direction, we are also examining the possibility of constructing a racetrack-shaped solenoid coil downstream of the bend with full aperture of 48×66 cm^2.

The parameters of the bent-solenoid spectrometer magnet are summarized in Table 7.

Momentum Resolution of a Bent-Solenoid Spectrometer. A bent-solenoid spectrometer has a momentum resolution given by [93]

$$\frac{\sigma_P}{P} \approx \frac{P\sigma_x}{\theta_{\rm bend} e B_s L^{5/2}}\sqrt{\frac{720}{n}}, \tag{66}$$

when limited by position measurement accuracy σ_x. In this relation, L is the length over which the position measurements are made (active length of the TPC) and n is the number of measurements per unit length.

There is also a limit on resolution due to multiple scattering given by [93]

$$\frac{\sigma_P}{P} = \frac{13.6\ {\rm MeV}/c}{P\beta\theta_{\rm bend}}\sqrt{N_X}, \tag{67}$$

Table 7: Parameters of the analysis spectrometer magnet system. The length L_S includes both the bent and straight sections of the solenoid.

B_S	2 T
$R_{\rm bend}$	1.4 m
$\theta_{\rm bend}$	15°
$R_{S,\rm max}$	33 cm
L_S	1.4 m
B_G	0.714 T
$\Delta y_{G,\rm max}$	9 cm
$R_{\rm Larm,max}$	11.7 cm

where N_X is the number of radiation lengths of material encountered during the measurement.

While one can reduce multiple scattering by operating the tracking chamber at low pressure, this will limit the ability of the chamber to provide particle ID via dE/dx measurements. So we consider options to operate the chamber near atmospheric pressure, while minimizing multiple scattering but maintaining high ionization density.

Table 8 lists relevant parameters for candidate gas mixtures and for the component simple gases. TPC's have often operated with an AR/CH_4 (90/10) mixture because of its low saturation-drift voltage and reasonably good ionization density.

Table 9 includes the momentum resolution limits from eqs. (66-67) evaluated at the limits of the momentum range of interest in a chamber. Gas mixtures have been chosen for which the number n of samples/m is about 2,400. The chamber length is $L = 50$ cm and we assume the position resolution from a single cluster is $\sigma_x = 300$ μm.

We see that the Ar/CH_4 (90/10) gas mixture causes too much multiple scattering to obtain 5% momentum resolution at 100-MeV/c momentum. This suggests the use of an atmospherice-pressure helium/isobutane gas mixture, as has become popular at B-factories [94]. The price for this would be a rather high operating voltage for the TPC. Use of iC_4H_{10} at 225 Torr should permit twice as good momentum resolution as the Ar/CH_4 (90/10) mixture and the same dE/dx resolution, and requires operating the chamber at only 2.5 times higher voltage.

The TPC parameters are summarized in Table 10. For comparison, the TPC's under development for MUCOOL have a position accuracy of $\sigma_x = 200$ μm, measurement length $L = 43$ cm, $n = 33$ measurements per meter, and 0.0002 radiation lengths of material.

Table 8: Parameters for candidate chamber gases and their components, at STP and for minimum ionizing particles.

Parameter	He	Ar	CH_4	iC_4H_{10}	Ar/CH_4 (90/10)	He/iC_4H_{10} (75/25)
Atomic number	4	40	16	58		
Primary clusters/cm (STP)	4	25	25	84	25	25
Radiation lengths/m	0.0002	0.0091	0.0015	0.0059	0.0083	0.0016
Saturation E field (kV/cm)	–	–	0.9	1.5	0.2	≈ 1.5
Voltage for 50 cm (kV)	–	–	45	75	10	75
Saturation drift velocity (cm/μs)	–	–	10	5	6	3
Drift time over 50 cm (μsec)	–	–	5	10	8	17

Table 9: Limits on momentum resolution in the proposed spectrometer due to position resolution of the TPC's and to multiple scattering.

P (MeV/c)	β_π	Position ($n = 2400$/m)	Scattering Ar/CH_4 (90/10)	Scattering iC_4H_{10} (225 Torr)
100	0.58	0.0006	0.086	0.038
500	0.96	0.003	0.017	0.008

3.7.4 Particle Identification

Particle identification is an essential component of this experiment. Besides the pions and muons the outgoing flux will contain a substantial background of electrons and protons. In addition, we expect Kaon production (some of which is potentially useful as a source of muons) at approximately 10% of the pion rate. However, it is not necessary for our purposes to distinguish pions from muons; we ultimately desire to know the rate of captured muons, but essentially all pion decays result in muons that remained captured in the solenoid channel.

We plan to base the particle identification a combination of a threshold Čerenkov counter and dE/dx measurements from the TPC's. A time-of-flight system was considered but it is difficult to construct a "start" counter suitable for 100-MeV/c pions (32 keV) with the required precision.

Table 10: Parameters of the TPC's.

Radius (TPC_1)	24 cm
Area (TPC_2)	48×66 cm^2
L	50 cm
σ_x	300 μm
Gas	iC_4H_{10} @ 225 Torr
Voltage	25 kV
Charge samples (n)	2400/m
N_X	0.0016 rad. lengths
Drift time	8 μs
Readout time	10 ms

Additional particle identification will be provided by readout of the ionization density in the TPC. Each track will yield $\approx 2,400$ primary ionizations over the total of one meter of path length in the TPC,s corresponding to a dE/dx resolution of 5-6% (σ). Figure **??** shows data from BNL experiment E-910 for which a similar ionization density held [15]. Kaons and protons will be distinguished from pions and muons over the entire interval 100-500 MeV/c, and electrons are distinguished for momenta greater than about 250 MeV/c.

Electrons will be identified by a positive signal in an aerogel threshold Čerenkov counter. The β of a 500-MeV/c muon is 0.98, so the radiatior should have index about 1.01, as is now readily achieved in high-quality aerogels [97, 98, 99, 100, 101, 102, 103, 104, 105]. The aerogel would be subdivided into $5 \times 5 \times 15$ cm^3 cells, each viewed by a 3″-diameter Hamamatsu fine-mesh photomultiplier tube. A total of about 100 cells will cover the 48×66 cm^2 beam ellipse at the downstream end of the bent-solenoid channel.

A charged particle other than an electron has about 5% probablility of producing a knock-on electron that yields a signal in the aerogel detector. In view of the expected large number of low-energy protons in the spectrometer, the segmentation of the aerogel detector is justified.

In the system as described there would remain about a 5% loss of pions and muons below 250 MeV/c due to mistagging from knock-ons in the aerogel. This inefficiency could be reduced to 0.2% as the expense of a second layer of aerogel detectors.

3.7.5 Expected Rates and Running Time

We expect about 1 collected pions per interacting proton in the momentum range of interest [1].

If the readout time is 10 ms per event, and the beam spill is 400 ms long, then we will record about 40 events/pulse. With 10 pulses/hour (limited by the time for the pulsed 20-T solenoid to cool), we will obtain about 400 events/hour.

The TPC readout is to be based on the STAR TPC electronics, which incorporates analog storage of 512 time samples in switched-capacitor arrays. While there are about 1,200 primary ionizations per track in the TPC, it is not necessary to sample each ionization separately. It should suffice to allot about 50 samples per track, clock at 6 MHz, for a total of 85 μs. If the protons are separated by 10 or more time samples, *i.e.*, by 1.6 μs or more, we should be able to identify different protons easily. Equivalently, we can process 50 proton interactions per event with little time overlap among samples from different interactions. With this procedure, we can measure about 20,000 pions/hour.

These collected pions must be binned over the three phase variables P, r and ϕ. In addition, the field strength of the collection solenoid falls from 20-T to 18-T during the 400-ms beam spill. Thus the collected events must also be binned in magnetic field. If we require a total of 6 bins per variable, there are a total of $1,296$ bins. Then each 4-d bin receive only ≈ 15 events per hour. If we require $\approx 1,000$ events per bin to achieve 3% statistical accuracy, then we require ≈ 60 hours of beam operation. It should be emphasized, however, that during most of this time we do not need beam delivered to the experiment, so efficient operation in conjunction with other users may be possible.

3.8 Simulations of the Beam-Jet-Magnet Interaction

4 Budgets, Schedules, Personnel....

Table 11: Preliminary budget estimate by fiscal year. Funds are in units of 1M$.

Program Step	FY99	FY00	FY01	Total
1. Simple beam tests	0.12	–	–	0.12
2. Jet in 20-T magnet	0.08	–	–	0.08
3. Jet in beam	0.20	0.20	–	0.40
4. Add 20-T pulsed magnet	0.20	≈0.60	–	≈0.80
5. Add 70-MHz rf cavity	0.15	≈0.80	–	≈0.95
6. Add 1.25-T magnet	0.05	0.15	≈1.00	≈1.20
7. Characterize pion yield	0.05	0.10	≈1.85	≈2.00
8. Simulations	0.15	0.15	0.15	0.45
Total	1.00	≈2.00	≈3.00	≈**6.00M**

ID	Task Name	Duration	Cost	Start	Finish
1	**Targetry R&D**	**782 days**	**$6,000,000**	**Thu 10/1/98**	**Fri 9/28/01**
2	**Liquid Metal/Beam**	**55 days**	**$120,000**	**Thu 10/1/98**	**Wed 12/16/98**
3	Containment Vessel	45 days	$30,000	Thu 10/1/98	Wed 12/2/98
4	Instrumentation	45 days	$80,000	Thu 10/1/98	Wed 12/2/98
5	Test at AGS	10 days	$10,000	Thu 12/3/98	Wed 12/16/98
6	**Liquid Metal Jet I**	**85 days**	**$80,000**	**Thu 10/1/98**	**Wed 1/27/99**
7	Jet prototyping	60 days	$20,000	Thu 10/1/98	Wed 12/23/98
8	Instrumentation	75 days	$50,000	Thu 10/1/98	Wed 1/13/99
9	Test at FSU	10 days	$10,000	Thu 1/14/99	Wed 1/27/99
10	**Liquid Metal Jet II**	**190 days**	**$200,000**	**Thu 10/1/98**	**Wed 6/23/99**
11	Design	60 days	$20,000	Thu 10/1/98	Wed 12/23/98
12	Liquid Jet	45 days	$20,000	Thu 12/24/98	Wed 2/24/99
13	Containment Vessel	45 days	$20,000	Thu 12/24/98	Wed 2/24/99
14	Instrumentation	45 days	$20,000	Thu 12/24/98	Wed 2/24/99
15	Test at AGS, I	10 days	$10,000	Thu 2/25/99	Wed 3/10/99
16	AGS Extraction Upgrad	180 days	$100,000	Thu 10/1/98	Wed 6/9/99
17	Test at AGS, II	10 days	$10,000	Thu 6/10/99	Wed 6/23/99
18	**Pulsed Solenoid**	**450 days**	**$1,000,000**	**Mon 1/4/99**	**Fri 9/22/00**
19	Design	150 days	$80,000	Mon 1/4/99	Fri 7/30/99
20	Coil Purchase/Fabricati	160 days	$500,000	Mon 8/2/99	Fri 3/10/00
21	Assembly	50 days	$100,000	Mon 5/22/00	Fri 7/28/00
22	LN2 Cryostat Design	90 days	$50,000	Mon 8/2/99	Fri 12/3/99
23	LN2 Cryostat Fabricatio	50 days	$100,000	Mon 12/6/99	Fri 2/11/00
24	LN2 Handling	40 days	$20,000	Mon 3/27/00	Fri 5/19/00
25	Move/Refurbish PS	40 days	$40,000	Mon 8/9/99	Fri 10/1/99
26	Move Substation	40 days	$40,000	Mon 10/4/99	Fri 11/26/99
27	Substation Attachment	20 days	$20,000	Mon 11/29/99	Fri 12/24/99
28	Switching System	45 days	$30,000	Mon 4/3/00	Fri 6/2/00
29	Test at AGS	40 days	$20,000	Mon 7/31/00	Fri 9/22/00
30	**RF Systems**	**510 days**	**$1,300,000**	**Mon 3/1/99**	**Fri 2/9/01**
31	**RF Cavity**	**510 days**	**$930,000**	**Mon 3/1/99**	**Fri 2/9/01**
32	Design	150 days	$100,000	Mon 3/1/99	Fri 9/24/99
33	Purchase/Fabricat	200 days	$600,000	Mon 9/27/99	Fri 6/30/00
34	Assembly	20 days	$20,000	Mon 7/3/00	Fri 7/28/00
35	Testing I	60 days	$30,000	Mon 7/31/00	Fri 10/20/00
36	Refurbish/rebuild	20 days	$150,000	Mon 10/23/00	Fri 11/17/00
37	Testing II	60 days	$30,000	Mon 11/20/00	Fri 2/9/01
38	**Site Preparation**	**218 days**	**$170,000**	**Wed 8/18/99**	**Fri 6/16/00**
39	Design	30 days	$30,000	Wed 8/18/99	Tue 9/28/99
40	Blockhouse	60 days	$20,000	Fri 10/1/99	Thu 12/23/99
41	Shielding	60 days	$30,000	Fri 12/24/99	Thu 3/16/00
42	Power Service	70 days	$20,000	Fri 12/24/99	Thu 3/30/00
43	Vacuum	120 days	$50,000	Mon 1/3/00	Fri 6/16/00
44	DI Water	45 days	$20,000	Mon 1/3/00	Fri 3/3/00
45	**LBL Transfer**	**50 days**	**$50,000**	**Mon 3/1/99**	**Fri 5/7/99**
46	Testing	40 days	$40,000	Mon 3/1/99	Fri 4/23/99
47	Packing	5 days	$5,000	Mon 4/26/99	Fri 4/30/99
48	Shipping	5 days	$5,000	Mon 5/3/99	Fri 5/7/99
49	**Low Level RF**	**105 days**	**$40,000**	**Tue 6/1/99**	**Mon 10/25/99**

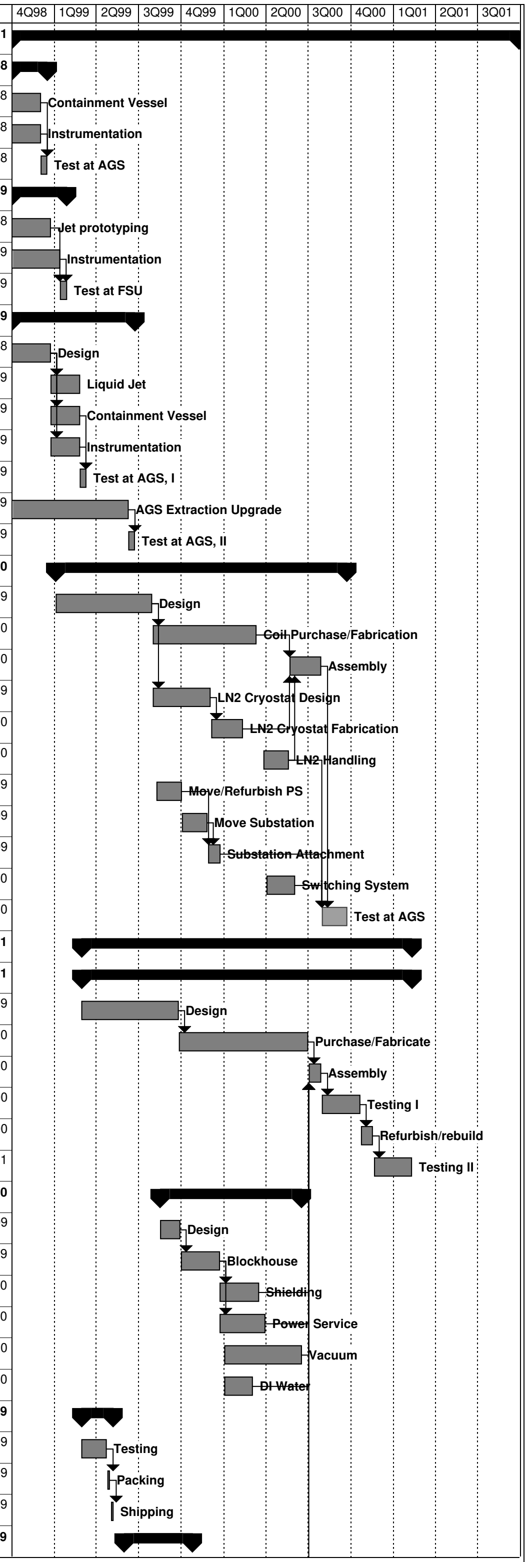

ID		Task Name	Duration	Cost	Start	Finish
50		Design	30 days	$10,000	Tue 6/1/99	Mon 7/12/99
51		Procurement	45 days	$20,000	Tue 7/13/99	Mon 9/13/99
52		Testing	30 days	$10,000	Tue 9/14/99	Mon 10/25/99
53		**Pulsing System**	**140 days**	**$110,000**	**Mon 10/4/99**	**Fri 4/14/00**
54		Design	60 days	$30,000	Mon 10/4/99	Fri 12/24/99
55		Procurment	60 days	$30,000	Mon 12/27/99	Fri 3/17/00
56		Crowbar	60 days	$30,000	Mon 12/27/99	Fri 3/17/00
57		Testing	20 days	$20,000	Mon 3/20/00	Fri 4/14/00
58		**RF Solenoid**	**480 days**	**$1,100,000**	**Mon 7/5/99**	**Fri 5/4/01**
59		Coil Design	120 days	$60,000	Mon 7/5/99	Fri 12/17/99
60		Coil Fabricate	300 days	$500,000	Mon 12/20/99	Fri 2/9/01
61		Iron Design	120 days	$60,000	Mon 12/20/99	Fri 6/2/00
62		Iron Fabricate	150 days	$200,000	Mon 6/5/00	Fri 12/29/00
63		Support Design	80 days	$40,000	Mon 6/5/00	Fri 9/22/00
64		Support Fabricate	100 days	$50,000	Mon 9/25/00	Fri 2/9/01
65		Block House	80 days	$20,000	Mon 10/4/99	Fri 1/21/00
66		Move/Refurbish PS	60 days	$30,000	Mon 1/24/00	Fri 4/14/00
67		Substation Attachment	20 days	$20,000	Mon 4/17/00	Fri 5/12/00
68		Assemble/Test	60 days	$120,000	Mon 2/12/01	Fri 5/4/01
69		**Capture Experiment**	**515 days**	**$1,750,000**	**Mon 10/4/99**	**Fri 9/21/01**
70		Bent Solenoid Design	60 days	$30,000	Mon 10/4/99	Fri 12/24/99
71		Bent Solenoid Fabricati	300 days	$500,000	Mon 12/27/99	Fri 2/16/01
72		Guide Dipole Design	30 days	$20,000	Mon 1/3/00	Fri 2/11/00
73		Guide Dipole Fabricatio	180 days	$150,000	Mon 2/14/00	Fri 10/20/00
74		Transition Magnet Desi	30 days	$20,000	Mon 2/14/00	Fri 3/24/00
75		Transition Magnet fabric	120 days	$100,000	Mon 3/27/00	Fri 9/8/00
76		Power Suplies	90 days	$100,000	Mon 10/2/00	Fri 2/2/01
77		TPC system	240 days	$240,000	Mon 6/5/00	Fri 5/4/01
78		TOF System	240 days	$120,000	Mon 6/5/00	Fri 5/4/01
79		PWCs and scintillators	80 days	$150,000	Mon 10/2/00	Fri 1/19/01
80		Electronics and DAQDa	150 days	$200,000	Mon 10/2/00	Fri 4/27/01
81		Counting Trailer	60 days	$60,000	Mon 10/2/00	Fri 12/22/00
82		Assemble/Test	100 days	$60,000	Mon 5/7/01	Fri 9/21/01
83		**Simulation**	**782 days**	**$450,000**	**Thu 10/1/98**	**Fri 9/28/01**
84		FY99	260 days	$150,000	Thu 10/1/98	Wed 9/29/99
85		FY00	261 days	$150,000	Fri 10/1/99	Fri 9/29/00
86		FY01	260 days	$150,000	Mon 10/2/00	Fri 9/28/01

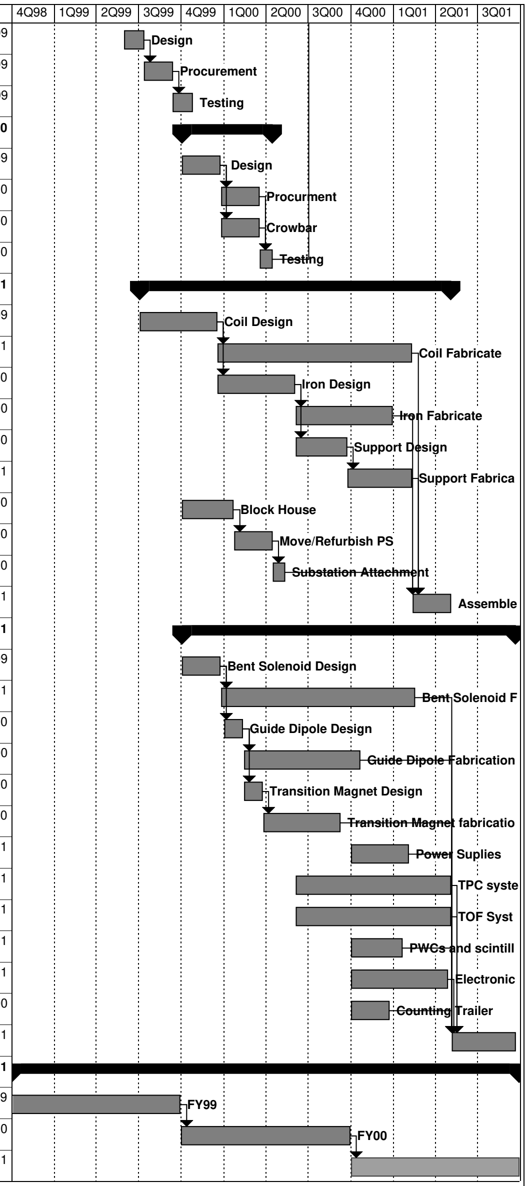

	4th Quarter	1st Quarter	2nd Quarter	3rd Quarter	4th Quarter	1st Quarter	2nd Quarter	3rd Quarter	4th Quarter	1st Quarter	2nd Quarter	3rd Quarter	Total
Targetry R&D													
Liquid Metal/Beam													
Containment Vessel	$30,000												$30,000
Instrumentation	$80,000												$80,000
Test at AGS	$10,000												$10,000
Liquid Metal Jet I													
Jet prototyping	$20,000												$20,000
Instrumentation		$50,000											$50,000
Test at FSU		$10,000											$10,000
Liquid Metal Jet II													
Design	$20,000												$20,000
Liquid Jet		$20,000											$20,000
Containment Vessel		$20,000											$20,000
Instrumentation		$20,000											$20,000
Test at AGS, I		$10,000											$10,000
AGS Extraction Upgrade			$100,000										$100,000
Test at AGS, II			$10,000										$10,000
Pulsed Solenoid													
Design		$26,649	$27,495	$25,856									$80,000
Coil Purchase/Fabrication				$35,000		$465,000							$500,000
Assembly								$100,000					$100,000
LN2 Cryostat Design					$50,000								$50,000
LN2 Cryostat Fabrication					$12,820	$87,180							$100,000
LN2 Handling							$20,000						$20,000
Move/Refurbish PS					$40,000								$40,000
Move Substation					$40,000								$40,000
Substation Attachment					$20,000								$20,000
Switching System							$30,000						$30,000
Test at AGS								$20,000					$20,000
RF Systems													
RF Cavity													
Design				$100,000									$100,000
Purchase/Fabricate							$600,000						$600,000
Assembly								$20,000					$20,000
Testing I									$30,000				$30,000
Refurbish/rebuild									$150,000				$150,000
Testing II										$30,000			$30,000
Site Preparation													
Design				$30,000									$30,000
Blockhouse					$20,000								$20,000
Shielding						$30,000							$30,000
Power Service						$20,000							$20,000
Vacuum							$50,000						$50,000
DI Water						$20,000							$20,000
LBL Transfer													
Testing			$40,000										$40,000
Packing			$5,000										$5,000
Shipping			$5,000										$5,000
Low Level RF													
Design				$10,000									$10,000
Procurement				$20,000									$20,000
Testing					$10,000								$10,000
Pulsing System													
Design					$30,000								$30,000
Procurment					$247,500	($217,500)							$30,000
Crowbar					$247,500	($217,500)							$30,000
Testing						$2,180	$17,820						$20,000
RF Solenoid													
Coil Design					$60,000								$60,000
Coil Fabricate										$500,000			$500,000
Iron Design							$60,000						$60,000
Iron Fabricate									$200,000				$200,000
Support Design								$40,000					$40,000
Support Fabricate										$50,000			$50,000
Block House						$20,000							$20,000
Move/Refurbish PS							$30,000						$30,000
Substation Attachment							$20,000						$20,000
Assemble/Test											$120,000		$120,000
Capture Experiment													
Bent Solenoid Design					$30,000								$30,000
Bent Solenoid Fabrication										$500,000			$500,000
Guide Dipole Design						$20,000							$20,000
Guide Dipole Fabrication									$150,000				$150,000
Transition Magnet Design						$20,000							$20,000
Transition Magnet fabrication								$100,000					$100,000
Power Suplies										$100,000			$100,000
TPC system											$240,000		$240,000
TOF System											$120,000		$120,000
PWCs and scintillators										$150,000			$150,000
Electronics and DAQData acquisition											$200,000		$200,000
Counting Trailer									$60,000				$60,000
Assemble/Test												$60,000	$60,000
Simulation													
FY99				$150,000									$150,000
FY00								$150,000					$150,000
FY01												$150,000	$150,000
Total	$160,000	$156,649	$187,495	$370,856	$807,820	$249,360	$827,820	$430,000	$590,000	$1,330,000	$680,000	$210,000	$6,000,000

5 Appendix A: BNL E-910, Low-Momentum Pion Production

Inclusive pion cross sections in proton nucleus interactions are quite hard to calculate due to the contribution of many different processes and are best determined experimentally. Various event generator codes used by the heavy ion physics community [11, 12, 14] to simulate the cascade inside the nucleus indicate a pronounced peak in pion production at low momenta. Unfortunately, there is very limited data in the literature for pion production at the low end of the spectrum (below 200 MeV/c). This data is also essential for calibrating the event generators for use in a realistic simulation of the muon collider front end.

Since many aspects of the targetry and pion capture/phase rotation depend on the shape and magnitude of these spectra, the muon collider collaboration has allocated some resources for getting critical results on pion production by joining AGS experiment 910 [15] which was capable of the necessary acceptance and statistics.

Experiment 910 ran for 14 weeks in the A1 beamline at the AGS during Spring 1996 using a proton beam on a target placed in the MPS spectrometer and collected about 20 million events of which about a quarter are minimum bias triggers for inclusive cross section measurements. The targets were varied in material (Be, Cu, Au, U) and thickness (2-100% of an interaction length) and three different beam energies were used (6, 12.5 and 18 GeV/c).

The main tracking detector was the EOS TPC placed inside the MPS magnet downstream of the target to achieve almost full forward acceptance for charged tracks, an accurate determination of the vertex position using these tracks and particle identification using ionization energy loss in the gas volume. It was supplemented by proportional chambers placed upstream for incoming beam track reconstruction as well as drift chambers, a Čerenkov counter and a time of flight wall located downstream for improved momentum resolution and particle ID. A scintillating-fiber detector behind the target was used as a multiplicity trigger for central collisions and a scintillator beam veto behind the TPC for minimum-bias events, including interactions that occur in the TPC gas.

This was the first and only run of this experiment so far and the efforts of the E910 collaboration have since been focused on careful analysis of the large data sample obtained. An early tracking pass over a fraction of the data for preliminary physics insight has been performed in March-April 1997. A calibration pass was completed through August-October 1997, a tracking pass over all the data using the calibration constants obtained and many improvements in tracking is underway and should be complete in Fall 98. The data processing effort is being carried out in parallel at many sites including BNL, Columbia, FSU, Iowa State, LLNL and ORNL.

By combining large acceptance with particle identification and high statistics, data from E910 has allowed a systematic study of proton nucleus interactions using different experimental handles like the number of slow protons and pions produced, rapidity loss of the leading particle, total transverse energy content, *etc.*

Reliable tracking of particles down to 50 MeV/c and below has been accomplished in offline analysis. An important aspect of the pion measurement in E910 is that the dE/dx sampling in the TPC is the only means of identification for particles below about 500 MeV/c since they either don't reach any detectors downstream of the TPC or the momentum is not high enough for particle ID using time of flight or Čerenkov light. There is a large amount of overlap in the electron and pion dE/dx bands around 100-200 MeV/c. The electrons are produced mostly from gamma conversions to e^+e^- pairs in the target which has enough radiation lengths to make the electron-to-pion ratio about 1:1 in this momentum region for the 2%-interaction-length Au target. This is dealt with in tracking by reconstructing e^+e^- pairs based on their small opening angle. The current tracking pass will produce better dE/dx resolution based on accurate TPC calibration and will allow better identification for pions.

An important question in interpreting results and validating event generators is whether the very slow large-angle/backward component of the pion spectrum is significant. This will be addressed using E910 data by looking at beam-gas interactions in the TPC. Although the TPC gas (P10) constitutes a very small amount of material in the beam path, the fraction of events with these interactions is still enough to generate a usable data set with full 4π coverage for tracks produced in proton-Ar interactions and will supply valuable information on this issue.

A publication on inclusive pion production based on E910 data is in preparation and will come out later this year. Comparison with event generators is also underway.

6 Appendix B: High Intensity Performance and Upgrades at the AGS

[This Appendix has been published separately as Ref. [91].]

6.1 Recent AGS High Intensity Performance

Figure 26 shows the present layout of the AGS-RHIC accelerator complex. The high intensity proton beam of the AGS is used both for the slow-extracted-beam (SEB) area with many target station to produce secondary beams and the fast-extracted-beam (FEB) line used for the production of muons for the g-2 experiment and for high intensity target testing for the spallation neutron sources and muon production targets for the muon collider. The same FEB line will also be used for the transfer of beam to RHIC.

The proton beam intensity in the AGS has increased steadily over the 35-year existence of the AGS, but the most dramatic increase occurred over the last couple of years with the addition of the new AGS Booster [110, 111]. In Fig. 27 the history of the AGS intensity improvements is shown and the major upgrades are indicated. The AGS Booster has one quarter the circumference of the AGS and therefore allows four Booster beam pulses to be stacked in the AGS at an injection energy of 1.5-1.9 GeV. At this increased energy, space-charge forces are much reduced and this in turn allows for the dramatic increase in the AGS beam intensity.

The 200-MeV LINAC is being used both for the injection into the Booster as well as an isotope production facility. A recent upgrade of the LINAC rf system made it possible to operated at an average H^- current of 150 μA and a maximum of 12×10^{13} H^- per 500-μs LINAC pulse for the isotope production target. Typical beam currents during the 500-μs pulse are about 80 mA at the source, 60 mA after the 750-keV RFQ, 38 mA after the first

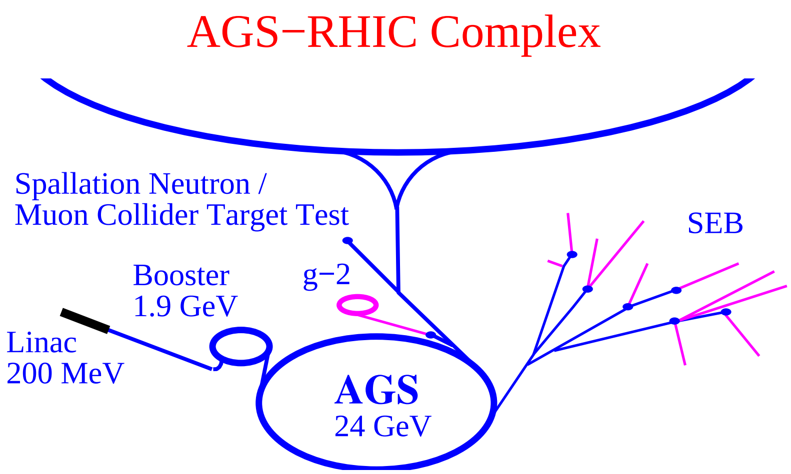

Figure 26: The AGS-RHIC accelerator complex.

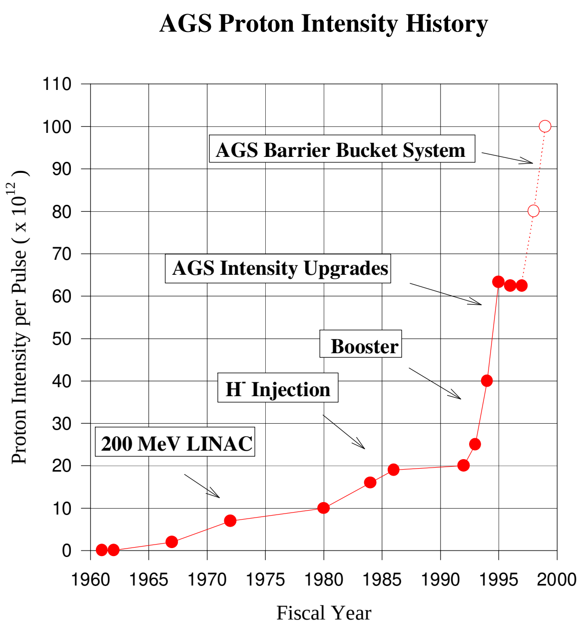

Figure 27: The evolution of the proton beam intensity in the Brookhaven AGS.

LINAC tank (10 MeV), and 37 mA at end of the LINAC at 200 MeV. The normalized beam emittance is about 2π mm-mrad for 95% of the beam and the beam energy spread is about ± 1.2 MeV. A magnetic fast chopper installed at 750 keV allows the shaping of the beam injected into the Booster to avoid excessive beam loss.

The beam intensity achieved in the Booster surpassed the design goal of 1.5×10^{13} protons per pulse and reached a peak value of 2.3×10^{13} protons per pulse. This was achieved by very carefully correcting all the important nonlinear orbit resonances, especially at the injection energy of 200 MeV, and by using the extra set of rf cavities that were installed for heavy-ion operation as a second harmonic rf system. The second-harmonic rf system allows for the creation of a flattened rf bucket which gives longer bunches with lower space-charge forces. The fundamental-rf system operated with 90 kV and the secondary-harmonic with 30 kV. The typical bunch area was about 1.5 eV-s. Even with the second-harmonic rf system the incoherent space-charge tune shift can reach one unit right at injection (3×10^{13} protons, norm. 95% emittance: 50π mm-mrad, bunching factor: 0.5). Of course, such a large tune shift is not sustainable, but the beam emittance growth and beam loss can be minimized by accelerating rapidly during and after injection. Best conditions are achieved by ramping the main field during injection with 3 T/s increasing to 9 T/s after about 10 ms. The quite large nonlinear fields from eddy currents in the Iconel vacuum chamber of the Booster are passively corrected using correction windings on the vacuum chamber that are driven by backleg windings [112].

The AGS itself also had to be upgraded to be able to cope with the higher beam intensity. During beam injection from the Booster, which cycles with a repetition rate of 7.5 Hz, the AGS needs to store the already transferred beam bunches for about 0.4 s. During this time the beam is exposed to the strong image forces from the vacuum chamber, which causes beam loss from resistive-wall-coupled bunch-beam instabilities within as short a time as a few hundred revolutions. A very powerful feedback system was installed that senses any transverse movement of the beam and compensates with a correcting kick. This transverse damper can deliver ± 160 V to a pair of 50-Ω, one-meter-long striplines. A recursive digital notch filter is used in the feedback circuit to allow for accurate determination of the average beam position and increased sensitivity to the unstable coherent beam motion. This filter design is particular important for the betatron tune setting of about 8.9 which is required to avoid non-linear octupole stopband resonance at 8.75. With an incoherent tune shift at the AGS injection energy of 0.1 to 0.2 it is still necessary, however, to correct the octupole stopband resonances to avoid excessive beam loss.

To reduce the space-charge forces further the beam bunches in the AGS are lengthened by purposely mismatching the bunch-to-bucket transfer from the Booster and then smooth the bunch distribution using a high-frequency 100-MHz dilution cavity. The resulting reduction of the peak current helps both with coupled bunch instabilities and stopband beam losses.

During acceleration the AGS beam has to pass through the transition energy after which the revolution time of higher energy protons becomes longer than for the lower energy protons. This potentially unstable point during the acceleration cycle was crossed very quickly with a new powerful transition-energy-jump system with only minimal losses even at the highest intensities. The large lattice distortions introduced by the jump system prior to the transition crossing severely limits the available aperture of the AGS in particular for momentum spread. Efforts to correct the distortions using sextupoles have been partially successful [113]. After the transition energy, a very rapid, high-frequency instability developed which could only be avoided by purposely further increasing the bunch length using again the high-frequency dilution cavity.

The peak beam intensity reached at the AGS extraction energy of 24 GeV was 6.3×10^{13} protons per pulse also exceeding the design goal for this latest round of intensity upgrades. It also represents a world record beam intensity for a proton synchrotron. With a 1.6-s slow-extracted-beam spill the average extracted beam current was about 3 μA. This level of performance was reached quite consistently over the last few years and during a typical 20 week run a total of 1×10^{20} protons are accelerated in the AGS to the extraction energy of 24 GeV.

At maximum beam intensity about 30% of the beam is lost at Booster injection (200 MeV), 25% during the transfer from Booster to AGS (1.5 GeV), which includes losses during the 0.4-s storage time in the AGS, and about 3% is lost at transition (8 GeV). Although activation levels are quite high all machines can still be manually maintained and repaired in a safe manner.

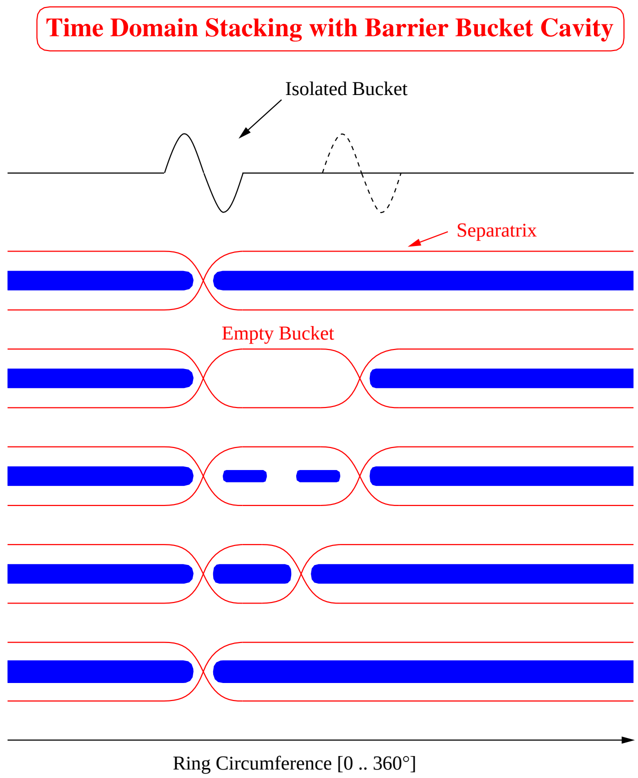

Figure 28: Time-domain-stacking scheme using a barrier-bucket cavity. The evolution of the longitudinal beam structure during the stacking process is shown from top to bottom.

6.2 Possible Future AGS Intensity Upgrades

Currently the number of Booster beam pulses that can be accumulated in the AGS is limited to four by the fact that the circumference of the AGS is four times the circumference of the Booster. This limits the maximum beam intensity in the AGS to four times the maximum Booster intensity which itself is limited to at most 2.5×10^{13} protons per pulse by the space-charge forces at Booster injection. To overcome this limitation some sort of stacking will have to be used in the AGS. The most promising scheme is stacking in the time domain. To accomplish this, a cavity that produces isolated rf buckets can be used to maintain a partially debunched beam in the AGS and still leave an empty gap for filling in additional Booster beam pulses. The stacking scheme is illustrated in Fig. 28. It makes use of two isolated rf buckets to control the width of this gap. Isolated bucket cavities, also called Barrier Bucket cavities, have been used elsewhere [114]. However, for this stacking scheme, a high rf voltage will be needed to contain the large bunch area of the high-intensity beam. An additional important advantage of this scheme is that while the beam is partially debunched in the AGS the beam density and therefore space-charge forces are reduce by up to a factor of two. A successful test of this scheme has recently been completed [115] and two 40-kV Barrier cavities are being installed in the AGS with the aim of accumulating six Booster beam pulses in the AGS to reach an intensity of about 1×10^{14} protons per pulse.

For further increases in the intensity the space-charge forces at Booster injection represent the main limitation. This could be overcome by an energy upgrade of the LINAC to about 600 MeV by replacing part of the present 200-MHz cavities with higher gradient 400-MHz cavities driven by klystrons. At 600 MeV the space-charge limit at Booster injection would be 5×10^{13} protons per pulse or 2×10^{14} protons in the AGS for 4 cycles per AGS cycle.

As more Booster beam pulses are accumulated in the AGS the reduction in the overall duty cycle becomes more significant. For fast-extracted-beam operation (FEB) the accumulation of four Booster pulses already contributes significantly to the overall cycle time. With the addition of a 2-GeV accumulator ring in the AGS tunnel this overhead time could be completely avoided. Such a ring could be built rather inexpensively using low-field magnets. The maximum repetition rate of the Linac and Booster is 10 Hz. Since the circumference of the AGS is four times that of the Booster a repetition rate of 2.5 Hz would maintain a throughput of 80 μA through the whole accelerator chain. Such an increase of the AGS repetition rate by a factor of 2.5 could be achieved by an upgrade of the AGS main magnet power supply only. The resulting beam power of 2 MW at 25 GeV corresponds to the required proton driver performance needed for a demonstration muon collider project. The upgrades to the AGS complex are summarized in Fig. 29.

7 References

[1] C.M. Ankenbrandt *et al.*, *Status of Muon Collider Research and Development and Future Plans*, submitted to Phys. Rev. Sp. Top. – Acc. Beams;
http://www.cap.bnl.gov/mumu/status_report.html

[2] The $\mu^+\mu^-$ Collider Collaboration, *$\mu^+\mu^-$ Collider Feasibility Study*, BNL-52503, FERMILAB-Conf-96/092, LBNL-38946 (July 1996);
http://www.cap.bnl.gov/mumu/book.html

[3] A. A. Kolomensky, *On the Oscillation Decrements in Accelerators in the Presence of Arbitrary Energy Losses*, Sov. Atomic Energy **19**, 1511 (1965);
http://puhep1.princeton.edu/mumu/physics/kolomensky/1.html

[4] Yu. M. Ado and V. I. Balbekov, *Use of Ionization Friction in the Storage of Heavy Particles*, Sov. Atomic Energy **31**, 731 (1971);
http://puhep1.princeton.edu/mumu/physics/ado/1.html

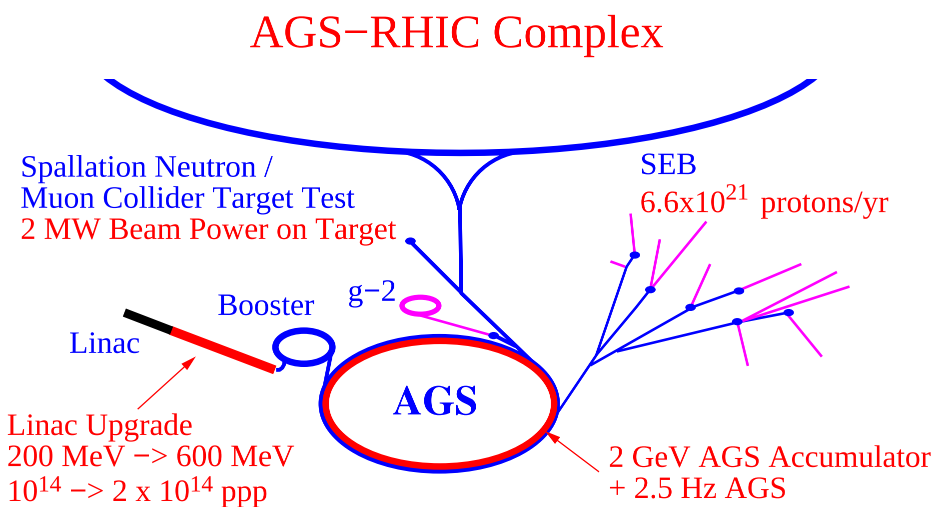

Figure 29: Summary of intensity upgrades for the AGS.

[5] The main Web page of the Muon Collider Collaboration is at
http://www.cap.bnl.gov/mumu/mu_home_page.html

[6] The MUCOOL Collaboration, *Ionization Cooling Research and Development Program for a High Luminosity Muon Collider*, FNALl-P904 (April 15, 1998);
http://www.fnal.gov/projects/muon_collider/

[7] R. Noble N. Mokhov and A. Van Ginneken, *Target and Collection Optimization for Muon Colliders*, FERMILAB-Conf-96/006 (January 1996);
http://www-ppd.fnal.gov/muscan/munotes/MC-031.pdf

[8] D. Ehst, N. V. Mokhov, R. J. Noble and A. Van Ginneken, *Target Options and Yields for a Muon Collider Source*, Proc. PAC97 (Vancouver, 1997), p. 393;
http://www.triumf.ca/pac97/papers/pdf/4W023.PDF

[9] H. Takahashi, Y. An, X. Chen and M. Nomura, *Optimization of the Target for Muon Colliders*, Proc. PAC97 (Vancouver, 1997), p. 402;
http://www.triumf.ca/pac97/papers/pdf/4W027.PDF

[10] N.V. Mokhov and A. Van Ginneken, *Pion Production and Targetry at $\mu^+\mu^-$ Colliders*, FERMILAB-Conf-98/041 (January 1998);
http://www-ap.fnal.gov/~mokhov/papers/1998/Fermilab-Conf-98-41.ps

[11] S.H. Kahana, Y. Pang and T.J. Schlagel, in *Proceedings of Heavy Ion Physics at the AGS-HIPAGS '93*, eds. G.S. Stephans, S.G. Steadman and W.E. Kehoe; D. Kahana and Y. Torun, *Analysis of Pion Production Data from E-802 at 14.6 GeV/c Using ARC*, BNL-61983 (July 1995); see also
http://bnlnth.phy.bnl.gov/arc/arc.html

[12] N.V. Mokhov, *The MARS Code System Userś Guide*, Fermilab-FN-628 (1995); http://www-ap.fnal.gov/MARS/

[13] N.V. Mokhov and S.I. Striganov, *Model for Pion Production in Proton-Nucleus Interactions*, FERMILAB-Conf-98/053 (Feb. 5, 1998); http://www-ap.fnal.gov/~mokhov/papers/1998/Fermilab-Conf-98-53.ps

[14] J. Ranft, *DPMJET version II.3 and II.4*, INFN-AE-97-45 (1997); http://preprints.cern.ch/cgi-bin/setlink?base=preprint&categ=scan&id=SCAN-9711078.

[15] Experiment E-910 at BNL-AGS; http://www.nevis.columbia.edu/heavyion/e910/

[16] J. Lettry *et al.*, *Experience with ISOLDE Molten Metal Targets at the CERN-PS Booster*, in Proceedins of ICANS-XIII (1995); http://puhep1.princeton.edu/mumu/target/

[17] G.I. Silvestrov, *Liquid Metal Jet Targets for Intense High Energy Beams*, Budker Institute preprint (Aug. 1998); http://puhep1.princeton.edu/mumu/silvestrov/jet_silvestrov.pdf

[18] C. Johnson, *Solid and Liquid Targets Overview*, Proceeding of the Mini-Workshop: Target and Muon Collection Magnets and Accelerators, (Oxford, MS, 1997, unpublished); http://nicewww.cern.ch/~cdj/public/mumutarg/

[19] C. Lu and K. T. McDonald, Low-Melting-Temperature Metals for possible Use as Primary Targets at a Muon Collider Source, Princeton/$\mu\mu$/97-3 (1998); http://puhep1.princeton.edu/mumu/mumu-97-3.ps

[20] R. Weggel, *Deceleration of Conductor by Magnetic Field: 1) Paraxial; 2) Perpendicular*, CAP-220-MUON-98R (1998).

[21] C. Lu and K.T. McDonald, *Flowing Tungsten Powder for Possible Use as the Primary Target at a Muon Collider Source*, Princeton/$\mu\mu$/98-10 (Mar. 15, 1998); http://puhep1.princeton.edu/mumu/mumu-98-10.ps

[22] B.J. King, N.V. Mokhov and R. Weggel, *A Cu-Ni Rotating Band Target for Pion Production at Muon Colliders*, http://pubweb.bnl.gov/people/bking/target_aps98/index.html

[23] R. Weggel, *4-MW Hollow-Conductor Magnets for 20 T Hybrid Systems to Collect Pions for a Muon Collider*, BNL-Technical Report MU-015 (Jan. 1997).

[24] J.R. Miller *et al.*, IEEE Trans. Magnetics **30**, 1563 (1994).

[25] R.B. Palmer and J.C. Gallardo, *MC, Fortran program to simulate the front end and cooling section*, (unpublished).

[26] D. Neuffer and A. van Ginneken, (private communication, 1998).

[27] See p. 220 of ref. [2].

[28] H. Kirk, (private communication, 1997).

[29] K. Assamagan *et al.*, *Measurement of the muon momentum in pion decay at rest using a surface muon beam*, Phys. Lett. **B335**, 231 (1994).

[30] B. Norum and R. Rossmanith, *Polarized beams in a muon collider*, Nucl. Phys. B (Proc. Suppl.) **51A**, 191 (1996).

[31] G.S. Bauer, *ESS Liquid Metal Target Studies*, ESS 95-33-T (Oct. 1995).

[32] G.S. Bauer, *Mercury as a Target Material for Pulsed (Fast) Spallation Neutron Sources*, ICANS-XIII, PSI-Proceedings 95-02 (Oct. 1995), p. 547.

[33] T. A. Gabriel *et al.*, *The National Spallation Neutron Source Target Station: A General Overview*, Proc. PAC97 (Vancouver, 1997), p. 86;
http://www.triumf.ca/pac97/papers/pdf/2B012.PDF

[34] *Target Systems*, Chap. 5 of the National Spallation Neutron Source Conceptual Design Report (NSNS/CDR-2, May 1997);
http://www.ornl.gov/~nsns/CDRDocuments/CDRSections/Sect5.pdf

[35] J.R. Haines, *Comparison of Liquid and Solid Targets for Pulsed Spallation Neutron Sources*, ORNL report NSNS/TSR0009 (July 1997).

[36] D.B. Cline, ed., *Proceedings of the High Intensity Targeting Workshop*, (Fermilab, April 28-30, 1980).

[37] J.A. Hassberger, *Flowing Liquid Lithium Target*, in [36], p. 12.

[38] R.J. Stefanski, *A Study in Target Design*, in [36], p. 41.

[39] *Feasibility Study into the Development of a Liquid Metal Pulsed Current Target for ACOL*, Report No. C2365/F, Contract No: R/785.985/PS/AA (Cambridge Consultants Ltd., Cambridge, U.K., 1985).

[40] Z. Tang and K. Anderson, *Shock Waves in $\bar{p}$ Target* Fermilab/TN-1763 (Nov. 1991).

[41] K. Skala and G.S Bauer, *On the Pressure Wave Problem in Liquid Metal Targets*, ICANS-XIII, PSI-Proceedings 95-02 (Oct. 1995).

[42] B.R. Appleton and G.S. Bauer, *Proc. of the Int. Workshop on the Technology and Thermal Hydraulics of Heavy Liquid Metals (Hg, Pb, Bi and Their Eutectics)*, (Schruns, Austria, Mar. 1996), ORNL CONF-9603171 (June 1996).

[43] R.P. Taleyarkhan, S.H. Kim and J.R. Haines, *Modelling & Analysis of AGS Thermal Shock Experiment*, ORNL report.

[44] R.P. Taleyarkhan, F. Moraga and C.D. West, *Experimental Determination of Cavitation Thresholds in Liquid Water and Mercury*, Proc. 2nd Int. Topical Meeting on Accel. Applications, AccApp'98, (Gatlinburg, TN, Sept. 1998); ORNL report.

[45] R.P. Taleyarkhan *et al.*, *Results of Thermal-Shock Modeling & Analyses for the National Spallation Neutron Source*, in *Proc. Topical Meeting on Nuclear Applications of Accelerator Technology*, (Albuquerque, NM, Nov. 1997), p. 293.

[46] L. Ni and G. Bauer, *Dynamic Stress of a Liquid Metal Target Container under Pulsed Heating*, PSI report (1998);
http://puhep1.princeton.edu/mumu/target/bauer/1.html

[47] J.R. Haines, *A Simple figure of Merit for Comparison of Thermal Shock Capabilities of Candidate Target Materials*, ORNL report NSNS/TSR5 (Mar. 3, 1997).

[48] D.H. Trevena, *Cavitation and Tension in Liquids* (Adam Hilger, Bristol, U.K., 1987).

[49] F.R. Young, *Cavitation* (McGraw-Hill, New York, 1989).

[50] T.G. Leighton, *The Acoustic Bubble* (Academic Press, San Diego, 1994).

[51] A. Kovacs, *Estimating the Full-Scale Tensile, Flexular and Compressive Strength of First-Year Ice*, CRREL Report 96-6 (Sept. 1996), Fig. 9;
http://www.crrel.usa.ce.army.mil/techpub/CRREL_Reports_web/reports/CR96_11.pdf

[52] L. Briggs, *Limiting Negative Pressure of Water*, J. Appl. Phys. **21**, 721 (1950).

[53] D.A. Wilson, J.W. Hoyt and J.W. McKane, *Measurement of tensile strength of liquids by an explosion technique*, Nature **253**, 723 (1975).

[54] *Design Report TEVATRON 1 Project*, Fermilab (Sept. 1984).

[55] J.. Lettry *et al.*, article in preparation (1998).

[56] H. Ullmaier and E. Carsughi, *Radiation damage problems in high power spallation neutron sources*, Nucl. Instr. and Meth. **B101**, 406 (1995).

[57] T.W. Eaton *et al.*, *Conducting Targets for $\overline{p}$ Production of ACOL. Past Experience and Prospects*, IEEE Trans. Nuc. Sci. **NS-32**, 3060 (1985).

[58] *Autopsie d'Une Cible en Cuivre*, CERN Central Workshop Metallurgy Dept. Report No. 3103 (1984).

[59] *Etude d'Une Cible a Antiprotons en Plomb*, CERN Central Workshop Metallurgy Dept. Report No. 3198 (1984).

[60] *Metallographic Examination of a Lightly Irradiated Copper/Graphite/Aluminium Target for CERN*, Report No. EIR KT: 7.423.0284, Federal Institute for Reactor Research (Wuerenlingen, Switzerland, 1984).

[61] R. Horne, *Preliminary Post-Irradiation Examination of a Rhenium "Snout" Target*, CERN Remote Handling Section (1985), unpublished; copy with C. Johnson).

[62] *High Temperature Compatibility Between Materials for Pulsed Current Targets*, Report No. OEFZS-A-0852 WE-402/86 (Osterreichisches Forschungzentrum, Seibersdorf, Austria, 1986).

[63] S.C. O'Day and f.M. Bienosek, *8-9 GeV $\bar{p}$ yield measurements at the Fermilab antiproton source*, Nucl. Instr. and Meth. **A343**, 343 (1994).

[64] Günter Bauer,private communication.

[65] R.N. Lyon (ed.), *Liquid Metals Handbook*, 2nd ed., NAVEXOS-P.733 (June 1952, revised 1954); *Liquid Metals*, in *Reactor Handbook*, 2nd ed., C.R. Tipton, Jr., (ed.), Interscience, New York, 1960), p. 994.

[66] *Materials for Spallation Neutron Sources*, Proceedings of the Workshop held at Los Alamos National Laboratory (Feb. 6-10, 1995), ed. by A. Longshore, LA-13097; http.//lib-www.lanl.gov/la-pubs/00285851.pdf

[67] J.R. DiStefano, *A Review of the Compatibility of Containment Materials with Potential Liquid Metal Targets*, ORNL-TM-13056 (Aug. 1995).

[68] D. Filges, R.D. Neef and H. Schaal, *Nuclear Studies of Different Target Systems for ESS*, ICANS-XIII, PSI-Proceedings 95-02 (Oct. 1995), p. 537.

[69] L. Briggs, *Limiting Negative Pressure of Mercury in Pyrex Glass*, J. Appl. Phys. **24**, 488 (1953).

[70] A. des Brasunas, *Interim Report on Static Liquid-Metal Corrosion*, ORNL/TM1646 (May 11, 1954).

[71] J.V. Cathcart and W.D. Manly, *The Mass Transfer Properties of Various Metals and Alloys in Liquid Lead*, Corrosion **12**(2), 43 (Feb. 1956).

[72] A.J. Romano, C.J. Kamut and D.H. Gurinsky, *The Investigation of Container Materials for Bi and Pb Alloys. Part I. Thermal Convection Loops*, BNL-811 (T-313) (July 1963).

[73] G.M. Tolsen and A. Taboda, *A Study of Lead and Lead-Salt Corrosion in Thermal-Convection Loops*, ORNL/TM-1437 (April 1966).

[74] J.R. Weeks, *Lead, Bismuth, Tin and Their Alloys as Nuclear Coolants*, Nucl. Eng. and Des. **15**, 363 (1971).

[75] J.R. DiStefano and O.B. Cavin, *Temperature Gradient Compatibility Tests of Some Refactory Metals and Alloys in Bismuth and Bismuth-Lithium Solution*, ORNL/TM-5503 (Nov. !976).

[76] H. Baker (ed.), *Alloy Phase Diagrams*, 2nd ed., Vol. III of the ASM handbook (ASM International, Materials Park, OH, 1997).

[77] J. Yahia and J.P. Thobe, *The Temperature Dependence of the Resistivity of Liquid Gallium to 1000°C*, Can. J. Phys. **50**, 2554 (1972).

[78] R.K. Smither *et al.*, *Liquid gallium cooling of silicon crystals in high intensity photons beams*, Rev. Sci. Instrum. **60**, 1486 (1989).

[79] R.K. Smither *et al.*, *Recent experiments with liquid gallium of crystal diffraction optics*, Rev. Sci. Instrum. **63**, 1746 (1992).

[80] J. Walker and W.H. Wells, *Drag Force on a Conducting Spherical Drop in a Nonuniform Magnetic Field*, ORNL/TN-6976 (Sept. 1979).

[81] Lord Rayleigh, *The Theory of Sound* (reprinted by Dover, 1945), Vol. 2, p. 362.

[82] R. Criss and F.E. Rose, *Spatial and Temporal Development of Emissions from an Exploding Mercury Jet*, IEEE Trans. Plasma Sci. **23**, 145 (1995).

[83] W.E. Ansley, S.A. Merryman and F.E. Rose, *Characterization of Liquid Mercury Jets and the Potential Application as an Opening Switch*, (1995).

[84] W.E. Ansley F.E. Rose, *Evaluatiopn of Liquid-Metals Jets as the Conductor in a Rep-Rated, Exploding-Fuse Opening Switch*, IEEE Trans. Magnetics **32**, 1980 (1996).

[85] S. Chandrasekhar, *Hydrodynamic and Hydromagnetic Stability* (reprinted by Dover, 1981), §112.

[86] C. Ankenbrandt *et al.*, *Bunching Near Transition in the AGS*, Phys. Rev. ST Accel. Beams **1**, 030101 (1998);
http://www-lib.fnal.gov/archive/1998/pub/Pub-98-006.html

[87] J. Norem *et al.*, *An AGS experiment to test bunching for the proton driver of the muon collider*, ANL-HEP-CP-98-32 (May 1998).

[88] J. Norem *et al.*, *Bunch Shortening Experiments in the Fermilab Booster and the AGS*, Proc. PAC97 (Vancouver, 1997);
http://www.triumf.ca/pac97/papers/pdf/4W024.PDF

[89] J. Norem *et al.*, *The Proton Driver for the $\mu^+\mu^-$ Collider*, Proc. PAC97 (Vancouver, 1997);
http://www.triumf.ca/pac97/papers/pdf/4W025.PDF

[90] T. Roser, *AGS Performance and Upgrades: A Possible Proton Driver for a Muon Collider*, AIP Conf. Proc. **372**, 47 (1996);
ftp://ftp.mumu.bnl.gov/pub/documents/roser.ps

[91] T. Roser, *High Intensity Performane and Upgrades as the Brookhaven AGS*, Proc. Workshop on Space Charge Physics in High Intensity Hadron Rings, (Shelter Island, NY, May 4-7, 1998).

[92] D.D. Earl, J.R. Haines and C.C. Tsai. *Measurement of Strain Experience by a Mercury Target Vessel*, ORNL report SNS/TSR-0040 (1998).

[93] C. Lu, K. T. McDonald, E. J. Prebys and S. E. Vahsen, *A Detector Scenario for the Muon Cooling Experiment*, Princeton/$\mu\mu$/97-8 (May, 1998);
http://www.hep.princeton.edu/mumu/mumu-97-8.ps

[94] BaBar *Technical Design Report*, SLAC-R-95-497 (March, 1995), Table 5.6.

[95] E. Kichimi *et al.*, *The Čerenkov correlated timing detector. Beam test results from quartz and acrylic bars*, Nucl. Instr. and Meth. **A371**, 91 (1996).

[96] S.E. Vahsen and K.T. McDonald, *Precision Timing via Čerenkov Radiation*, Princeton/$\mu\mu$/98-11 (July 25, 1998);
http://puhep1.princeton.edu/mumu/timing.pdf

[97] R. Enomoto *et al.*, *Feasibility Study of Single-Photon Counting Using a Fine-Mesh Phototube for an Aerogel Readout* Nucl. Instr. and Meth. **A332**, 129 (1993)

[98] I. Adachi *et al.*, *Study of a threshold Čerenkov counter based on silica aerogels with low refractive indices*, Nucl. Instr. and Meth. **A355**, 390 (1995); http://xxx.lanl.gov/ps/hep-ex/9412008

[99] T. Nozaki *et al.*, Nucl. Phys. B (Proc. Suppl.) **50**, 288 (1996).

[100] T. Iijima *et al.*, *Aerogel Čerenkov counter for the BELLE experiment*, Nucl. Instr. and Meth. **A379**, 457 (1996).

[101] T. Iijima *et al.*, Nucl. Instr. and Meth. **A387**, 64 (1997).

[102] M. Hazumi *et al.*, Nucl. Phys. B (Proc. Suppl.) **59**, 61 (1997).

[103] R. Suda *et al.*, *Monte-Carlo Simulation for an Aerogel Čerenkov Counter*, Nucl. Instr. and Meth. **A406**, 213 (1998); http://xxx.lanl.gov/ps/hep-ex/9707042

[104] M.H.R. Khan *et al.*, *The monitoring system for the aerogel Čerenkov counter of the BELLE detector*, submitted to Nucl. Instr. and Meth. http://xxx.lanl.gov/ps/hep-ex/9803027

[105] D.R. Marlow *et al.*, *BELLE Aerogel Čerenkov Counter Readout System Documents*; http://viper.princeton.edu/~marlow/acc/acc.html

[106] A. Hassanein, *Deuteron beam interaction with lithium jet in a neutron source test facility*, J. Nucl. Mater. **233-237**, 1547 (1996).

[107] A. Hassanein, *Disrupton Damage to Plasma-Facing Components from Various Plasma Instabilities*, Fusion Technol. **30**, 713 (1996).

[108] A. Hassanein *et al.*, *Modeling and simulation of melt-layer erosion during a plasma disruption*, J. Nucl. Mater. **241-243**, 288 (1997).

[109] A. Hassanein and I. Konkashbaev, *Dynamic Behavior of Plasma-Facing Materials during Plasma Instabilities in Tokamak Reactors*, Plasma Devices and Operations **5**, 297 (1988).

[110] M. Blaskiewicz *et al.*, *High Intensity Proton Operations at Brookhaven*, Proc. PAC95 (Dallas, Texas, 1995), p. 383.

[111] L. Ahrens *et al.*, *High Intensity Proton Acceleration at the Brookhaven AGS – An Update*, Proc. PAC97 (Vancouver, 1997), p. 89; http://www.triumf.ca/pac97/papers/pdf/7P001.PDF

[112] G.T. Danby and J.W. Jackson, Part. Accel. **27**, 33 (1990).

[113] W.K. van Asselt *et al.*, *The Transition Jump System*, Proc. PAC95 (Dallas, Texas, 1995), p. 3022.

[114] J.E. Griffin *et al.*, IEEE Trans. Nucl. Sci. **NS-30**, 3502 (1983).

[115] J.M. Brennan and M.M. Blaskiewicz, Proc. Workshop on Space Charge Physics in High Intensity Hadron Rings, (Shelter Island, NY, May 4-7, 1998).